

NASA TECHNICAL
MEMORANDUM

NASA TM X-53531

October 31, 1966

NASA TM X-53531

FACILITY FORM 602	N67 14461	
	(ACCESSION NUMBER)	(THRU)
	<u>43</u>	<u>1</u>
	(PAGES)	(CODE)
	<u>TMX-53531</u>	<u>29</u>
	(NASA CR OR TMX OR AD NUMBER)	(CATEGORY)

A PRELIMINARY REPORT ON ENERGETIC SPACE RADIATION AND
DOSE RATE ANALYSIS

by M. O. BURRELL, J. J. WRIGHT and J. W. WATTS

Research Projects Laboratory

NASA

*George C. Marshall
Space Flight Center,
Huntsville, Alabama*

GPO PRICE \$ _____

CFSTI PRICE(S) \$ _____

Hard copy (HC) 2.00

Microfiche (MF) 1.50

653 July 65

TECHNICAL MEMORANDUM X-53531

A PRELIMINARY REPORT ON ENERGETIC SPACE
RADIATION AND DOSE RATE ANALYSIS

By

M. O. Burrell, J. J. Wright and J. W. Watts

George C. Marshall Space Flight Center
Huntsville, Alabama

ABSTRACT

The purpose of this study is to present a compendium of the environmental data on trapped and untrapped radiation and the calculated tissue dose rates received from these radiations and their secondaries behind various shield thicknesses. Energetic radiation, as used here, refers to particles with energies greater than about 500 kilo-electron volts. The results given in this report should be of practical value for preliminary analysis of the radiation hazard to man during space flight.

NASA-GEORGE C. MARSHALL SPACE FLIGHT CENTER

NASA-GEORGE C. MARSHALL SPACE FLIGHT CENTER

TECHNICAL MEMORANDUM X-53531

A PRELIMINARY REPORT ON ENERGETIC SPACE
RADIATION AND DOSE RATE ANALYSIS

By

M. O. Burrell, J. J. Wright and J. W. Watts

RESEARCH PROJECTS LABORATORY
RESEARCH AND DEVELOPMENT OPERATIONS

TABLE OF CONTENTS

	Page
SUMMARY	1
INTRODUCTION	1
ACKNOWLEDGEMENT	2
THE GEOMAGNETIC FIELD AND CHARGED PARTICLE INTERACTIONS.	2
GALACTIC COSMIC RADIATION	5
SOLAR COSMIC RADIATION	6
PREDICTION OF SOLAR PROTON EVENTS	15
TRAPPED PROTON RADIATION	17
TRAPPED ELECTRON AND BREMSSTRAHLUNG RADIATION	21
CONCLUSIONS	27
REFERENCES.	33

LIST OF ILLUSTRATIONS

Figure	Title	Page
1.	Recent Satellite Version of the Magnetosphere Based on Results of IMP-1 Magnetic Field Experiment (November 27, 1963 to May 31, 1964)	3
2.	The Geometry of the B-L Coordinate System	4
3.	Variation of Proton Vertical Cutoff Energy during a Solar Active Period and as a Function of Earth Radii and Latitude during Quiet Time	5
4.	Galactic Cosmic Ray Differential Energy Spectrum and Proton Dose Rate Behind Aluminum Shields	6
5.	Typical Intensity-Time Profiles during a Solar Cosmic Ray Event (Taken from [7])	7
6.	Solar Proton Skin Dose Behind Aluminum Shields for Several Solar Flares	9
7.	Solar Proton Blood Dose Behind Aluminum Shields for Various Solar Cosmic Ray Events.	11
8.	Solar Proton Skin Dose Behind Polyethylene Shields for Seven Large Solar Cosmic Ray Events	11
9.	Comparison of Proton Skin Dose Using Masley and Webber Spectra	12
10.	Proton Skin Dose Behind Aluminum Shields for Various Characteristic Rigidity Values	14
11.	Monoenergetic Proton Dose as a Function of Depth Penetrated for Various Source Energy Spreads	14
12.	Characteristic Rigidity as a Function of Proton-to-Alpha Ratio (Taken from [10])	15

LIST OF ILLUSTRATIONS (Cont'd)

Figure	Title	Page
13.	A Comparison of Proton and Alpha Ray Skin Dose as a Function of Aluminum Shield Thickness	15
14.	Distribution of the Integrated Flux Per Event as a Function of the Number of Events for Solar Cycle 19 (Taken from [13])	17
15.	Monthly Probability of a Proton Event as a Function of Event Size (Taken from [13])	17
16.	Trapped Omnidirectional Proton Flux above 4 MeV	18
17.	Trapped Omnidirectional Proton Flux above 15 MeV.	18
18.	Trapped Omnidirectional Proton Flux above 34 MeV.	19
19.	Trapped Omnidirectional Proton Flux above 50 MeV.	19
20.	Trapped Proton Dose Rate as a Function of Shield Thickness and Altitude for 0-degree Inclination	20
21.	Trapped Proton Dose Rate as a Function of Shield Thickness and Altitude for 30-degree Inclination	20
22.	Trapped Proton Dose Rate as a Function of Shield Thickness and Altitude for 60-degree Inclination	20
23.	Trapped Proton Dose Rate as a Function of Shield Thickness and Altitude for 90-degree Inclination	20
24.	Trapped Electron Flux for Circular Orbits as a Function of Altitude and Orbit Inclination	21
25.	Electron Dose Rate as a Function of Altitude and Shield Thickness for 0-degree Inclination	23
26.	Electron Dose Rate as a Function of Altitude and Shield Thickness for 30-degree Inclination	23

LIST OF ILLUSTRATIONS (Cont'd)

Figure	Title	Page
27.	Electron Dose Rate as a Function of Altitude and Shield Thickness for 60-degree Inclination	24
28.	Electron Dose Rate as a Function of Altitude and Shield Thickness for 90-degree Inclination	24
29.	Bremsstrahlung Dose Rate as a Function of Shield Thickness and Altitude for 0-degree Inclination	25
30.	Bremsstrahlung Dose Rate as a Function of Shield Thickness and Altitude for 30-degree Inclination	25
31.	Bremsstrahlung Dose Rate as a Function of Shield Thickness and Altitude for 60-degree Inclination	26
32.	Bremsstrahlung Dose Rate as a Function of Shield Thickness and Altitude for 90-degree Inclination	26
33.	Electron and Bremsstrahlung Dose Rate as a Function of Shield Thickness Using a Typical Electron Integral Spectrum	27
34.	Electron Dose Rate as a Function of Shield Thickness for Several Characteristic E_0 Values	27
35.	Projected Electron Environment for December 1968	28
36.	Projected Electron Dose Rate as a Function of Altitude and Shield Thickness for 0-degree Inclination	29
37.	Projected Electron Dose Rate as a Function of Altitude and Shield Thickness for 30-degree Inclination.	29
38.	Projected Electron Dose Rate as a Function of Altitude and Shield Thickness for 60-degree Inclination.	30
39.	Projected Electron Dose Rate as a Function of Altitude and Shield Thickness for 90-degree Inclination.	30

LIST OF ILLUSTRATIONS (Concluded)

Figure	Title	Page
40.	Projected Bremsstrahlung Dose Rate as a Function of Altitude and Shield Thickness for 0-degree Inclination	31
41.	Projected Bremsstrahlung Dose Rate as a Function of Altitude and Shield Thickness for 30-degree Inclination	31
42.	Projected Bremsstrahlung Dose Rate as a Function of Altitude and Shield Thickness for 60-degree Inclination	32
43.	Projected Bremsstrahlung Dose Rate as a Function of Altitude and Shield Thickness for 90-degree Inclination	32

LIST OF TABLES

Table	Title	Page
I.	Integral Proton Flux (Protons/cm ² Flare) at 30 and 100 MeV with Corresponding Characteristic Rigidity p_0 and N_0	8
II.	Total Estimated Solar Flare Doses by Event for Ten Shielding Configurations	10
III.	Total Estimated Solar Flare Dose Behind Polyethylene Shields	12

TECHNICAL MEMORANDUM X-53531

A PRELIMINARY REPORT ON ENERGETIC SPACE RADIATION AND DOSE RATE ANALYSIS

SUMMARY

The results presented in this report should be of practical value for preliminary engineering analysis of space hazards and planning of possible space missions for either near-earth orbits or deep-space probes. The dose rate curves shown in this report are based on the latest environmental analysis by NASA and the United States Air Force. The environmental models and data will be continually updated as knowledge increases from better experimental data and more sophisticated analysis. As such modifications become available, the authors of this report intend to update the radiation dose rate analysis in future reports. This revision procedure is pertinent for the synchronous orbit radiation environment which is now being examined in greater detail by experimental space probes and theoretical analysis.

INTRODUCTION

This study is intended to present a compendium of the environmental data on trapped and untrapped radiation and the calculated tissue dose rates received from these radiations and their secondaries behind various shield thicknesses. Energetic radiation, as used here, refers to particles with energies greater than about 500 kilo-electron volts. The results given in this report should be of practical value for preliminary analysis of the radiation hazard to man during space flight.

It is the intention of the authors to update and expand the results and analysis presented in the following pages in a subsequent report. The updated reports will provide additional data for altitudes from 0 to 1852 kilometers (0-1000 nautical miles) and the synchronous orbit altitudes of 35,744 kilometers (19,300 nautical miles). Additional parametric studies will also be included in future reports.

The radiation environment consists of protons and electrons in the Van Allen belts and the energetic solar and galactic cosmic radiation. The solar wind is not included in this study since no appreciable dose is received behind any nominal shielding.

ACKNOWLEDGEMENT

The environmental data used in this report was taken primarily from the works of J. I. Vette of Aerospace Corporation and W. R. Webber of the Boeing Company.

THE GEOMAGNETIC FIELD AND CHARGED PARTICLE INTERACTIONS

The geomagnetic field around the earth forms a "magnetic pocket" known as the magnetosphere. The boundary of the magnetosphere is determined by the solar wind which is assumed to be a radial expansion of the sun's corona. At a certain radial distance above the earth, the geomagnetic field energy density equals the energy of the solar wind and there is a breakdown of the magnetic lines of force. This turbulent region is the magnetospheric boundary or transition zone. In the magnetosphere the magnetic field dominates, while outside the magnetosphere, the solar wind is the controlling energy mechanism.

The inner boundary of the transition region, called the magnetopause, occurs at about ten earth radii on the sunlit side of the earth, while the outer boundary of the transition region is in the form of a shock wave at about fourteen earth radii. The magnetopause around the earth in the form of an elongated teardrop with a long tail pointed away from the sun. Figure 1, taken from Ness [1], shows a recent version of the magnetosphere.

Perhaps the best way to represent the distribution of magnetically trapped particles about the earth is by using the B-L coordinate system employed by Carl McIlwain [2]. The B coordinate denotes the magnetic field strength at some specified point in space; L is the magnetic shell parameter that labels the shell upon which the guiding center of the trapped particle is adiabatically confined as it drifts around the earth. The L coordinate is approximately constant along a geomagnetic field line. In a dipole field, L is constant along the field

line and has the geometric property of being the equatorial distance from the dipole center to the magnetic field line. The geometry of the B-L coordinate

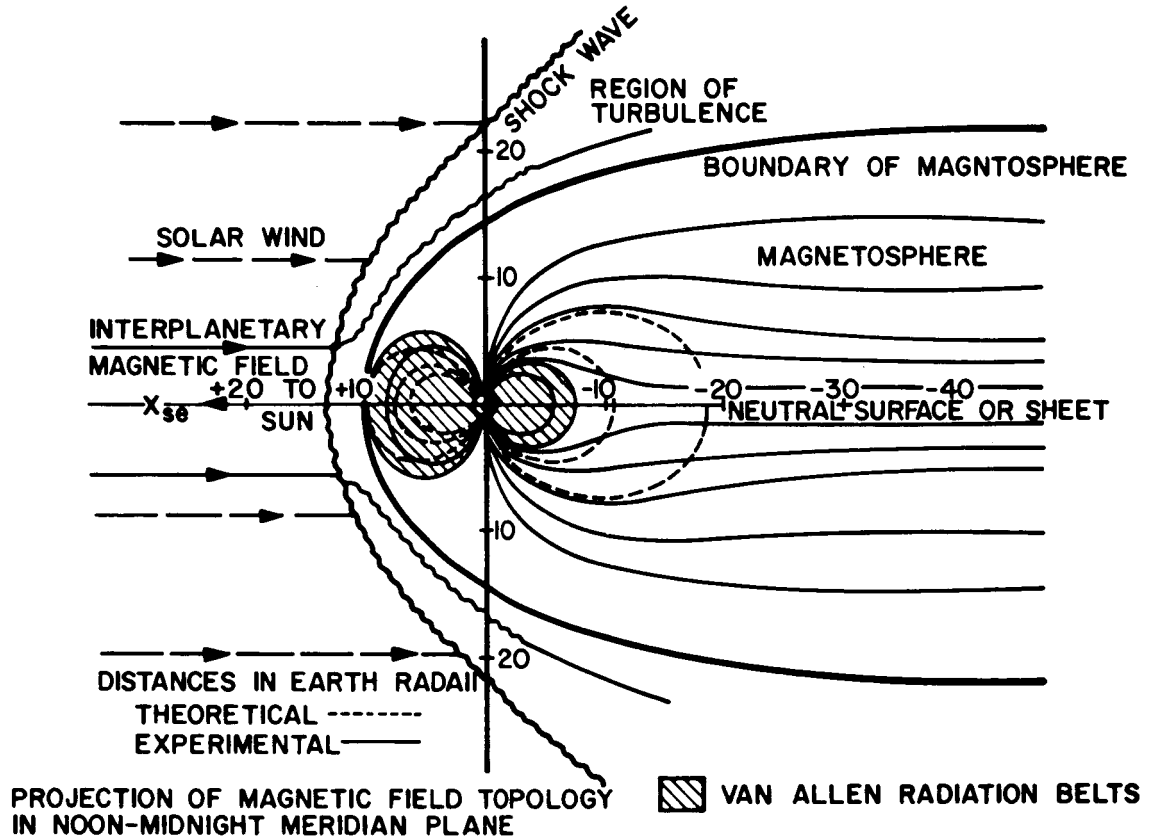


FIGURE 1. RECENT SATELLITE VERSION OF THE MAGNETOSPHERE
BASED ON RESULTS OF IMP-1 MAGNETIC FIELD EXPERIMENT
(NOVEMBER 27, 1963 TO MAY 31, 1964)

system is depicted in Figure 2. For a dipole field the B-L coordinates are related to the latitude and altitude of a point above the earth by the following:

$$B = \frac{M}{R^3} \left(4 - \frac{3R}{L} \right)^{\frac{1}{2}}, \quad L = \frac{R}{\cos^2 \lambda} \quad (1)$$

where M is the magnetic dipole moment ($0.311653 \text{ gauss } R_e^3$), R is the distance, in earth radii units, from the center of the earth, λ is the geocentric latitude and R_e is the radius of the earth. These relations should be used with caution since the earth's field cannot be depicted as a simple dipole.

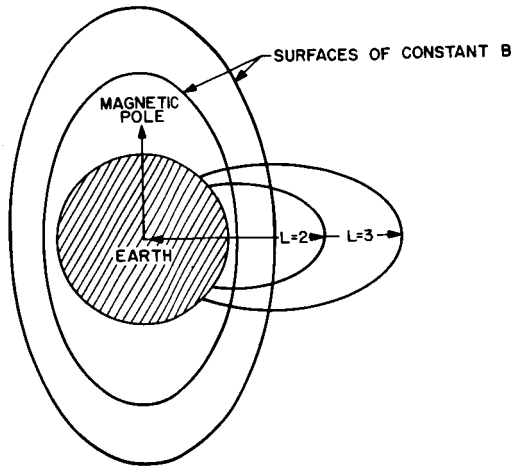


FIGURE 2. THE GEOMETRY OF THE B-L COORDINATE SYSTEM

The magnetic field of the earth alters the penetration of charged particles to the vicinity of the earth. The theory of the allowed cone of incident charged particles, as developed by Störmer [3], can be used as a basis for calculating the modification of an incoming energy spectrum from cosmic rays or solar flare protons. The theory is based on a dipole approximation of the geomagnetic field. The allowed cone is defined by:

$$p = \frac{15 \times 10^3 \cos^4 \lambda}{R^2 (1 + \sqrt{1 - \cos \gamma \cos^3 \lambda})} \quad (2)$$

where R , and λ are defined as in equation (1); p is the magnetic rigidity (momentum/charge) in megavolts (MV units); and γ is the half angle of the allowed cone about the normal to the meridian plane [4]. The magnetic rigidity in MV is related to the kinetic energy E in MeV of the particle as follows:

$$p(E) = \frac{\sqrt{E^2 + 2mc^2 E}}{ze} \quad (3)$$

where ze is the total charge, mc^2 is the particle rest mass energy (MeV); and E is expressed in MeV.

Combining equations (1), (2), and (3) for $\gamma = 90^\circ$, and solving for the kinetic energy E (MeV), the vertical cutoff energy for protons is found to be

$$E_c = -938 + \sqrt{(938)^2 + \frac{2.25 \times 10^8 \cos^8 \lambda}{R^4}} \quad (4)$$

The so-called vertical cutoff energy signifies that particles coming from the zenith and having energies greater than E_c will intercept a given point (R, λ) .

Figure 3 (left side) shows the variation of the vertical cutoff during solar active periods and quiet time [5]. A plot of the proton vertical cutoff energy is also shown in Figure 3 for various earth radii and latitudes for quiet times. The trapped radiation belts will be discussed further in later sections of this report.

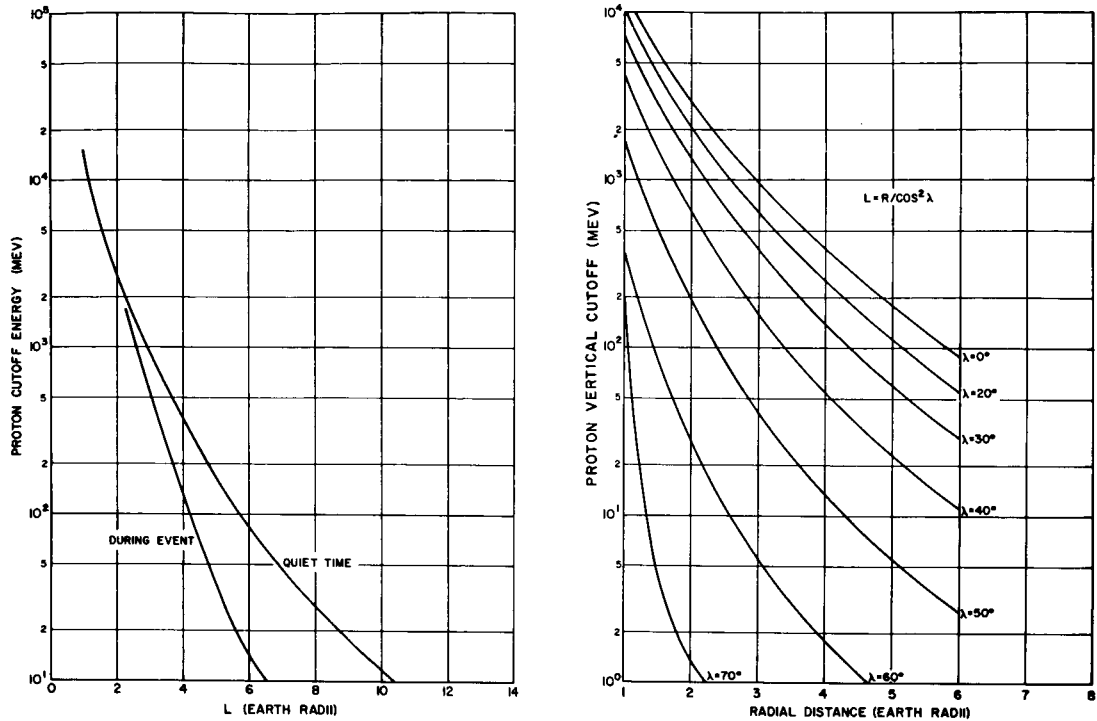


FIGURE 3. VARIATION OF PROTON VERTICAL CUTOFF ENERGY DURING A SOLAR ACTIVE PERIOD AND AS A FUNCTION OF EARTH RADII AND LATITUDE DURING QUIET TIME

GALACTIC COSMIC RADIATION

The galactic cosmic radiation is composed of about 85 percent protons, 14 percent alpha particles, and about 1 percent larger nuclei with energies ranging from 10^7 to 10^{19} eV, with an average energy of about 4 GeV. The proton flux at solar maximum is about 2 protons per square centimeter-second, and about twice this at solar minimum.

The differential energy spectrum [6] used for the dose rate calculations is shown in Figure 4. This spectrum has a questionable curvature below 500 MeV; a better representation will be obtained for future reports. The galactic cosmic ray dose rate (including secondaries) as a function of shield thickness at solar maximum and minimum is also depicted in Figure 4. If a spacecraft has an average thickness of about 6 grams per square centimeter of aluminum, the dose rate would be about 3.2 rads per year during solar maximum and about

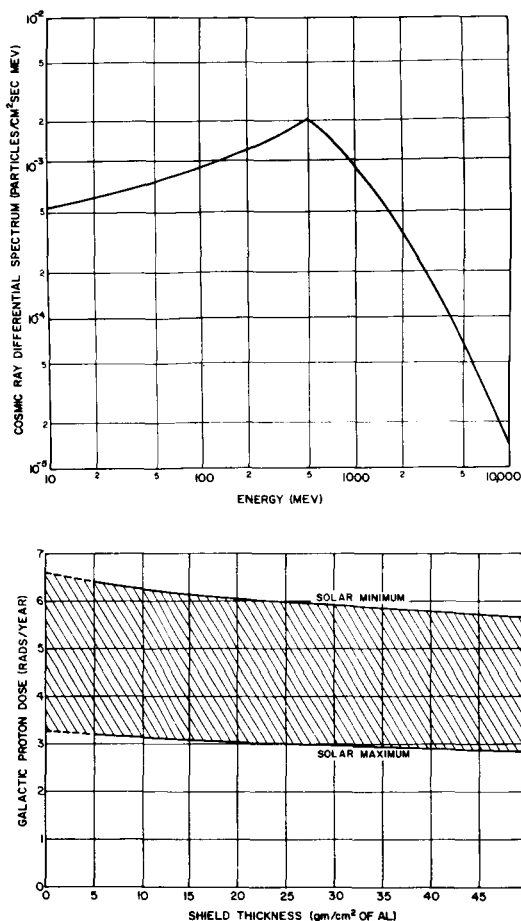


FIGURE 4. GALACTIC COSMIC RAY with a proton-to-alpha particle ratio DIFFERENTIAL ENERGY SPECTRUM varying from 1 to 100 and about 0.1 AND PROTON DOSE RATE BEHIND ALUMINUM SHIELDS percent of heavier nuclei.

The typical intensity-time profile for various rigidities in a solar cosmic ray event is shown in Figure 5 (Webber [7] provides detailed discussion). The intensity follows an exponential increase to I_{\max} at $t = 0$ and an exponential decay beyond maximum intensity. The integrated intensity above a given energy is calculated using the characteristic rise and decay times as

$$\begin{aligned}
 J(>E) &= \int_{-\infty}^0 I_{\max}(>E) \exp\left(-\frac{t}{t_R}\right) dt + \int_0^{\infty} I_{\max}(>E) \exp\left(-\frac{t}{t_D}\right) dt \\
 &= (t_R + t_D) I_{\max}(>E)
 \end{aligned}
 \tag{5}$$

twice this value during solar minimum, using the spectrum in Figure 4. Results by some writers have implied that the dose rate is higher by a factor of two; however, insufficient data on their proton energy spectrum makes a comparison impossible.

SOLAR COSMIC RADIATION

The radiation intensity from solar flare activity follows an approximate 11-year cycle with enormous flux variations ranging from about 10^5 protons per square centimeter at solar minimum to approximately 10^9 protons per square centimeter at solar maximum for protons with energy above 30 MeV. The solar radiation will also vary with distance from the sun. The following solar proton data are assumed to be at a radial distance of one astronomical unit.

The radiation from solar proton events is composed mainly of protons

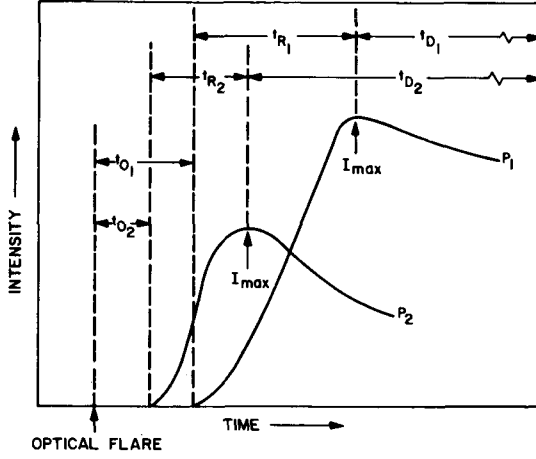


FIGURE 5. TYPICAL INTENSITY-TIME PROFILES DURING A SOLAR COSMIC RAY EVENT (TAKEN FROM [7])

To arrive at the differential spectrum of equation (6) in MeV units [8] , it is sufficient to use the relationship

$$p = \frac{1}{q} \sqrt{E^2 + 2ME} \quad (7)$$

and the Jacobian $\left| \frac{dp}{dE} \right|$ to obtain,

$$\phi(E) = \frac{N_0}{p_0} \exp\left(-\frac{p}{p_0}\right) \left| \frac{dp}{dE} \right| \frac{\text{particles}}{\text{cm}^2 - \text{MeV} - \text{Flare}}$$

or

$$\phi(E) = \frac{N_0}{p_0 q} \left(\frac{E + M}{\sqrt{E^2 + 2ME}} \right) \exp\left(-\frac{\sqrt{E^2 + 2ME}}{p_0 q}\right) \frac{\text{particles}}{\text{cm}^2 - \text{MeV} - \text{Flare}}$$

where p is the rigidity (momentum/charge) in MV units, E is kinetic energy (MeV); q is the charge, and M is the rest mass energy (MeV). Thus, for protons, $q = 1$, and $M = 938$ MeV; for alpha rays, $q = 2$, and $M = 3727$ MeV.

A list of the solar proton events [7] used in this study is shown in Table I. The solar proton events in Figure 6 represent the cases where the skin

where I_{\max} is the maximum intensity at time $t = 0$; t_R = rise time; and t_D = decay time.

The time integrated spectrum describing the flux for a given event is given by

$$J(>p) = N_0 \exp\left(-\frac{p}{p_0}\right) \quad (6)$$

where p_0 (MV) is the characteristic rigidity. N_0 is a constant determined from p_0 and $J(>p)$. Caution must be used in applying the same value of N_0 down to low rigidity values (< 30 MeV).

TABLE I. INTEGRAL PROTON FLUX (PROTONS/cm² FLARE) AT
30 AND 100 MeV WITH CORRESPONDING CHARACTERISTIC
RIGIDITY p_0 AND N_0

DATE	$J(>30\text{MEV})$	$J(>100\text{MEV})$	$P_0(\text{MV})$	N_0
2/23/56	1.0×10^9	3.5×10^8	195	3.41×10^9
8/3/56	2.5×10^7	6.0×10^6	144	1.32×10^8
1/20/57	2.0×10^8	7.0×10^6	61	1.02×10^{10}
8/29/57	1.2×10^8	3.0×10^6	56	8.49×10^9
10/20/57	5.0×10^7	1.0×10^7	127	3.30×10^8
3/23/58	2.5×10^8	1.0×10^7	64	1.04×10^{10}
7/7/58	2.5×10^8	9.0×10^6	62	1.18×10^{10}
8/16/58	4.0×10^7	1.6×10^6	64	1.67×10^9
8/22/58	7.0×10^7	1.8×10^6	56	5.02×10^9
8/26/58	1.1×10^8	2.0×10^6	51	1.21×10^{10}
9/22/58	6.0×10^6	1.0×10^5	50	7.21×10^8
5/10/59	9.6×10^8	8.5×10^7	84	1.67×10^{10}
7/10/59	1.0×10^9	1.4×10^8	104	1.00×10^{10}
7/14/59	1.3×10^9	1.0×10^8	80	2.59×10^{10}
7/16/59	9.1×10^8	1.3×10^8	105	8.92×10^9
4/1/60	5.0×10^6	8.5×10^5	116	3.93×10^7
4/28/60	5.0×10^6	7.0×10^5	104	5.01×10^7
5/4/60	6.0×10^6	1.2×10^6	127	3.96×10^7
5/13/60	4.0×10^6	4.5×10^5	94	5.09×10^7
9/3/60	3.5×10^7	7.0×10^6	127	2.31×10^8
9/26/60	2.0×10^6	1.2×10^5	73	5.29×10^7
11/12/60	1.3×10^9	2.5×10^8	124	8.98×10^9
11/15/60	7.2×10^8	1.2×10^8	114	5.89×10^9
11/20/60	4.5×10^7	8.0×10^6	118	3.44×10^8
7/11/61	3.0×10^6	2.4×10^5	81	5.77×10^7
7/12/61	4.0×10^7	1.0×10^6	56	2.83×10^9
7/18/61	3.0×10^8	4.0×10^7	102	3.13×10^9
7/20/61	5.0×10^6	9.0×10^5	120	3.66×10^7
9/28/61	6.0×10^6	1.1×10^6	121	4.33×10^7
10/23/62	1.2×10^5	1.0×10^4	83	2.13×10^7

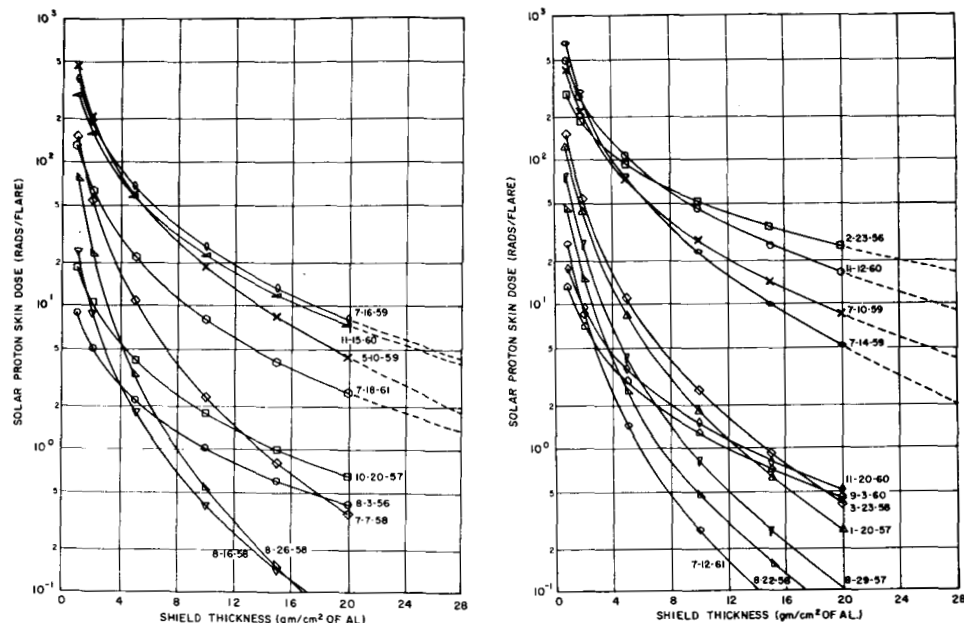


FIGURE 6. SOLAR PROTON SKIN DOSE BEHIND ALUMINUM SHIELDS FOR SEVERAL SOLAR FLARES

dose received behind 5 grams per square centimeter of aluminum shield is greater than about 1 rad. Figure 7 depicts solar cosmic ray doses at the blood forming organs. Table II presents a summary of the above graphs. The proton skin dose behind polyethylene shields for the seven largest solar cosmic ray events is shown in Figure 8 and summarized in Table III.

The radiation is assumed to be incident isotropically on a spherical shell of indicated shield thickness in the above calculations. The dose values given for solar protons include a correction for secondaries [8] and are given for a point detector at the center of the spherical shell. Since these results are point doses they are about a factor of two higher than an astronaut would actually receive. This difference results from the fact that self-shielding by the human body is not included in this type of calculation.

The November 12, 1960, proton spectral shape was somewhat controversial. The energy spectrum obtained by A. J. Masley [9] differs considerably from that of W. R. Webber (Table I) for energies below 100 MeV. Figure 9 is a comparison of skin doses using Webber's and Masley's energy spectra.

TABLE II. TOTAL ESTIMATED SOLAR FLARE DOSES BY EVENT
FOR TEN SHIELDING CONFIGURATIONS

DATE	SHIELDING CONFIGURATION									
	1/0*	2/0	5/0	10/0	20/0	1/5	2/5	5/5	10/5	20/5
2/23/56	280.00	181.00	91.80	50.20	24.80	64.78	58.00	43.75	30.40	17.90
8/3/56	8.50	5.00	2.20	1.00	0.40	1.39	1.21	0.85	0.53	0.27
1/20/57	122.00	43.50	8.30	1.80	0.30	3.42	2.57	1.23	0.46	0.11
8/29/57	77.00	25.10	4.20	0.80	0.10	1.63	1.20	0.54	0.19	0.04
10/20/57	18.50	10.30	4.10	1.80	0.70	2.53	2.17	1.46	0.88	0.41
3/23/58	148.00	53.60	10.90	2.50	0.40	4.67	3.55	1.75	0.69	0.17
7/7/58	150.00	53.70	10.50	2.30	0.40	4.38	3.30	1.60	0.61	0.15
8/16/58	23.70	8.60	1.80	0.40	0.10	0.75	0.57	0.28	0.11	0.03
8/22/58	45.00	14.90	2.50	0.50	0.10	0.96	0.71	0.32	0.11	0.02
8/26/58	75.00	23.10	3.40	0.50	0.10	1.19	0.85	0.36	0.11	0.02
5/10/59	470.00	211.10	59.30	18.30	4.40	30.18	24.28	13.60	6.70	2.10
7/10/59	420.00	214.00	73.20	27.40	8.40	41.56	34.65	21.76	11.84	4.80
7/14/59	650.00	284.50	75.90	22.30	5.00	37.56	30.00	16.75	7.80	2.50
7/16/59	382.00	194.80	67.20	25.30	7.80	38.30	31.98	20.16	11.03	4.50
9/3/60	13.00	7.20	2.90	1.20	0.50	1.77	1.52	0.10	0.06	0.03
11/12/60	484.00	269.60	105.50	44.90	16.20	64.53	55.12	36.87	21.83	10.05
11/15/60	288.00	151.90	55.90	22.40	7.50	30.04	27.91	18.14	10.33	4.49
11/20/60	17.30	9.50	3.60	1.50	0.05	2.14	1.82	1.20	0.69	0.31
7/12/61	25.70	8.40	1.40	0.30	0.03	0.54	0.40	0.18	0.06	0.01
7/18/61	128.00	64.20	21.60	8.00	2.40	12.16	10.11	6.30	3.39	1.35

* SHIELDING CONFIGURATIONS ARE GIVEN AS X/Y WHERE X = SHIELDING THICKNESS
IN g/cm² OF ALUMINUM AND Y = SHIELDING THICKNESS IN g/cm² OF TISSUE.

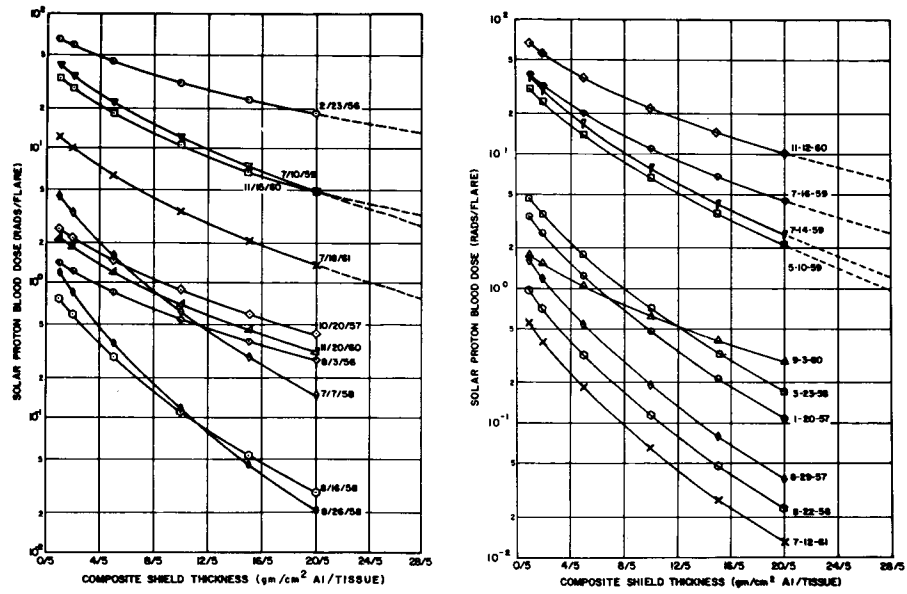


FIGURE 7. SOLAR PROTON BLOOD DOSE BEHIND ALUMINUM SHIELDS FOR VARIOUS SOLAR COSMIC RAY EVENTS

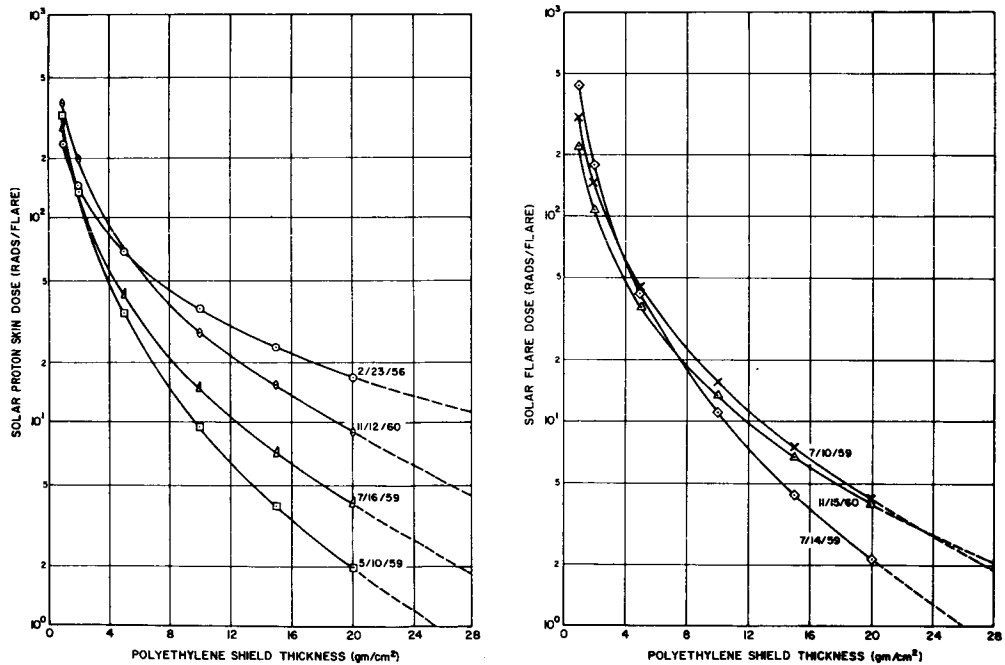


FIGURE 8. SOLAR PROTON SKIN DOSE BEHIND POLYETHYLENE SHIELDS FOR SEVEN LARGE SOLAR COSMIC RAY EVENTS

TABLE III. TOTAL ESTIMATED SOLAR FLARE DOSE BEHIND
POLYETHYLENE SHIELDS

SHIELD THICKNESS

DATE	1*	2	5	10	15	20
2/23/56	226.8	141.5	68.4	35.7	23.1	16.5
5/10/59	317.8	134.1	33.6	9.3	3.8	1.9
7/10/59	303.0	145.7	45.5	15.5	7.5	4.2
7/14/59	435.0	177.5	42.1	11.0	4.4	2.1
7/16/59	275.2	133.0	41.9	14.4	7.0	4.0
11/12/60	366.1	192.4	69.8	27.5	14.7	9.0
11/15/60	210.0	106.0	35.9	13.3	6.8	4.0

* SHIELD THICKNESS IN g/cm^2 OF POLYETHYLENE.

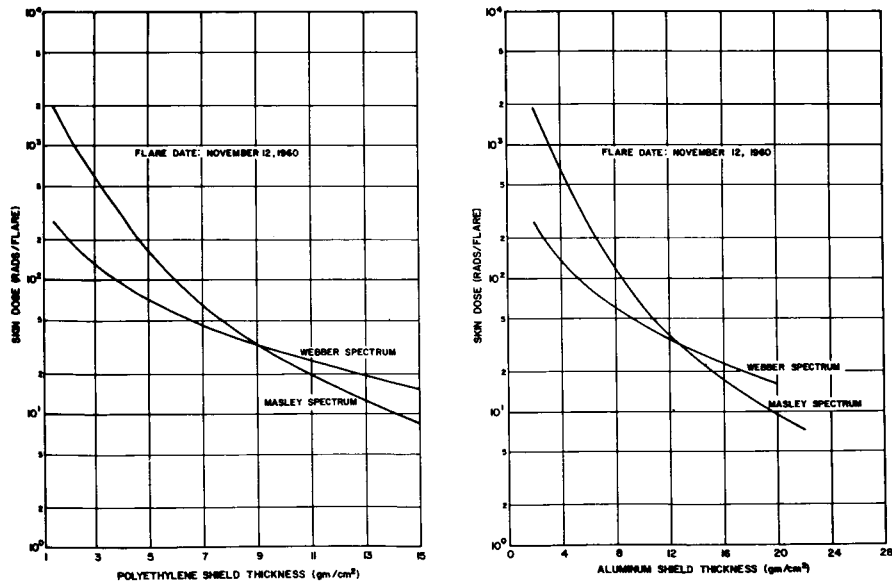


FIGURE 9. COMPARISON OF PROTON SKIN DOSE USING
MASLEY AND WEBBER SPECTRA

The differential energy spectrum used by Masley is given by

$$\begin{aligned}
 J(>E) &= 1.77 \times 10^{13} E^{-3} \text{ cm}^{-2} \text{ MeV}^{-1} (30 \leq E \leq 80 \text{ MeV}) \\
 J(>E) &= 9.62 \times 10^{16} E^{-5} \text{ cm}^{-2} \text{ MeV}^{-1} (80 \leq E \leq 440 \text{ MeV}) \\
 J(>E) &= 6.63 \times 10^{18} E^{-5.4} \text{ cm}^{-2} \text{ MeV}^{-1} (440 \leq E \leq 6600 \text{ MeV}).
 \end{aligned} \tag{8}$$

In comparing the results in the above figures, it should be noted that, using an aluminum shield of 6 grams per square centimeter, the dose at the blood-forming organs (5 centimeters of tissue) would be approximately the same for both spectra.

Figure 10 shows a parametric study of the dose received behind an aluminum shield for various values of the characteristic rigidity, p_0 . The proton integral spectrum in these calculations is given by

$$J(>p) = N_0 \exp\left(-\frac{p}{p_0}\right) = 10^9 \frac{\text{protons}}{\text{cm}^2} (E > 30 \text{ MeV}) \tag{9}$$

and the characteristic rigidity, p_0 , is given for values between 50 and 200 megavolts.

The experimental verification of proton dose rates (energy deposition) is not easily obtained for several reasons. One is that laboratory proton sources are usually monoenergetic, whereas flare sources are continuous energy spectra. Also, when a theoretical computation is made for a monoenergetic source, the energy band is depicted as a monoenergetic line; whereas, in the experiment the energy may have a 5 percent spread about the energy of interest. This energy spread in the source may have a much greater effect on the attempt to duplicate a theoretical result than is commonly believed. Figure 11 illustrates the difference in proton energy deposition for three different source energy spreads about an energy of 100 MeV in tissue and aluminum. The source was taken as 10^8 protons per square centimeter uniformly distributed in the energy band $100 \pm \Delta E$. The spiked curve was obtained by using an energy spread of only ± 0.005 MeV. This type of curve is characteristic of a theoretical calculation; whereas, the other curves of Figure 11 are typical of experimental results. The only effect considered in these calculations was an energy spread in the source.

Since the proton-to-alpha particle ratio for a solar flare ranges from 1 to 100, it may be important to determine the dose resulting from alpha particles.

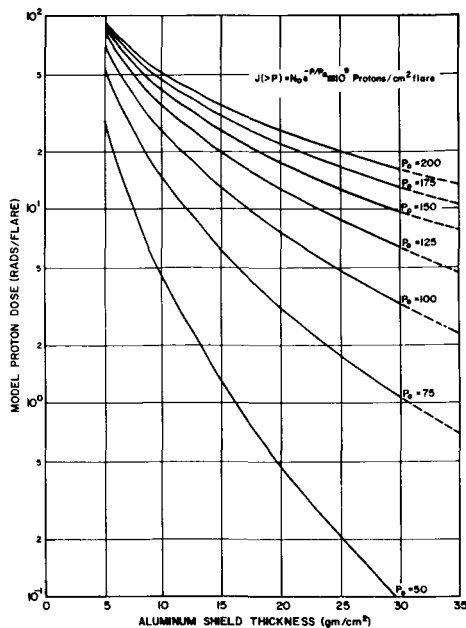


FIGURE 10. PROTON SKIN DOSE BEHIND ALUMINUM SHIELDS FOR VARIOUS CHARACTERISTIC RIGIDITY VALUES

The alpha particles seem to have about the same rigidity characteristics as the protons. Figure 12 illustrates the characteristic rigidity p_0 plotted as a function of proton-to-alpha ratio [10].

To evaluate the radiation dose derived from alpha rays, the large flare of July 10, 1959, was used. If alpha particles have the same rigidity as the protons, the proton-to-alpha ratio for the above flare is about 2. The alpha rays' integral spectrum is given by

$$J(>p) = 5 \times 10^9 \exp\left(-\frac{p}{104}\right) \frac{\text{alphas}}{\text{cm}^2\text{-Flare}} \quad (10)$$

Using the above alpha-ray energy spectrum, the proton and alpha-ray skin dose as a function of aluminum shield thickness are compared in Figure 13. For

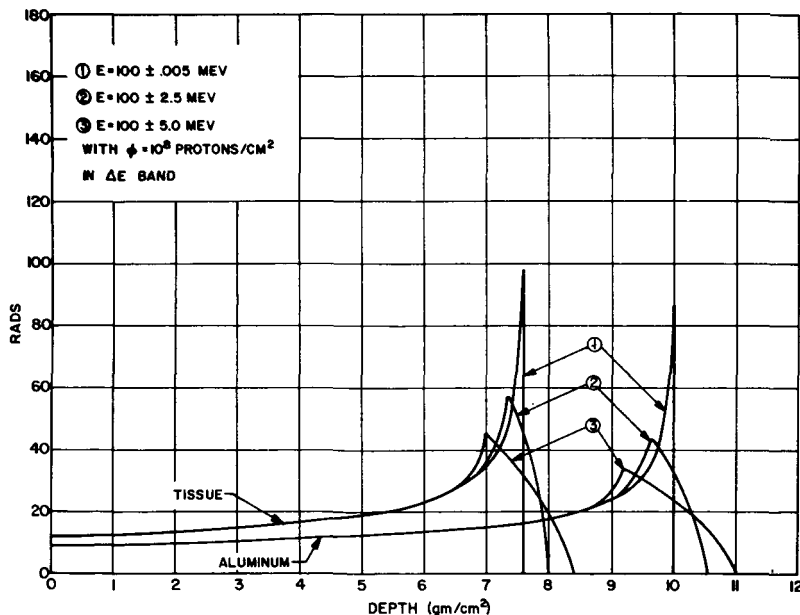


FIGURE 11. MONOENERGETIC PROTON DOSE AS A FUNCTION OF DEPTH PENETRATED FOR VARIOUS SOURCE ENERGY SPREADS

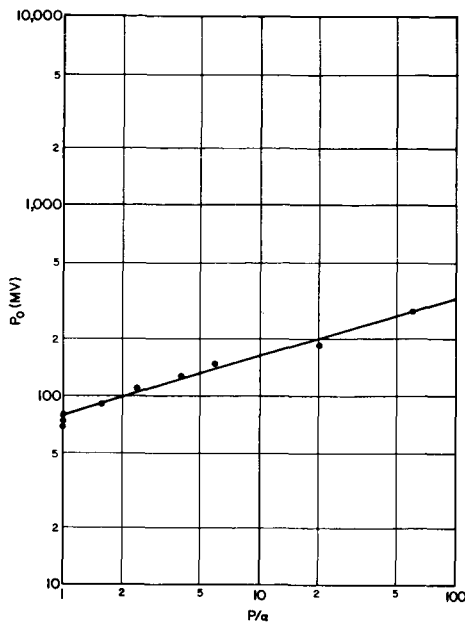


FIGURE 12. CHARACTERISTIC RIGIDITY AS A FUNCTION OF PROTON-TO ALPHA RATIO (TAKEN FROM [10])

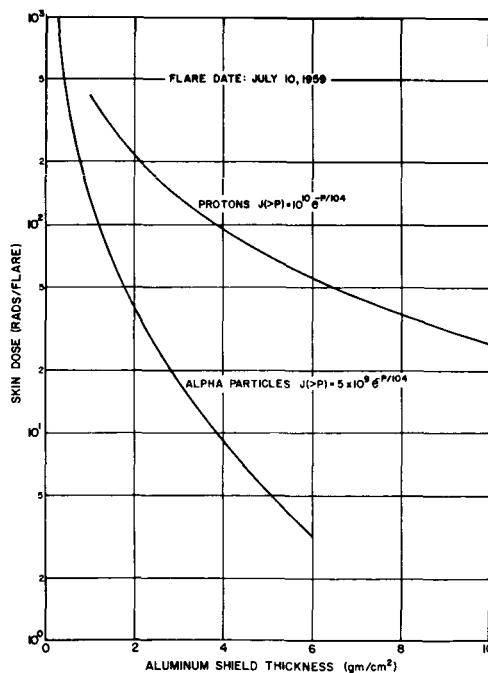


FIGURE 13. A COMPARISON OF PROTON AND ALPHA RAY SKIN DOSE AS A FUNCTION OF ALUMINUM SHIELD THICKNESS

an aluminum shield thickness of 4 grams per square centimeter, the proton dose is a factor of 10 above the alpha dose.

PREDICTION OF SOLAR PROTON EVENTS

Because of the importance of solar protons in the manned space flight program, it seems justifiable to discuss the methods and status of flare predictions. Many statistical studies have been undertaken, but not too much reliance can be placed on these studies because the sample of data is rather small. It should be pointed out that every flare differs from every other so that no exact relationship exists between observable features. A proper statistical analysis must involve a large number of events to permit specific statements about flare occurrence, duration and intensity.

Because of the rotation of the sun there exists an east-west asymmetry of solar proton events. For events occurring on the Eastern Hemisphere of the sun, the probability of having a solar proton event at the earth is one-third [7] that of events occurring on the Western Hemisphere. If an event does occur on the Eastern Hemisphere the corresponding onset, rise, and decay times are three times greater than events on the western half, giving astronauts more time to prepare for the oncoming event.

The presence and development of an active region with its associated sunspots and complex magnetic fields is a basic part of the process which leads

to a solar cosmic ray event. Thus, it is found that there are two aspects of primary importance for flare prediction [11] and warning capabilities. These are (1) the persistence of single active centers, and (2) the magnetic configurations of these active centers. With regard to (1), Guss [12] has pointed out that a single fixed location in solar longitude produced most of the major events in cycle 19. During a period of over 5 years (more than 73 rotations), several active centers grew and died in this same local region on the sun. These major events included the events of February 23, 1956, July 1959, November 1960, and July 1961, all occurring at the same location. About 75 percent of the total integrated particle intensity above 10 MeV came from this one "hot" location. According to Webber [7], over 90 percent of the output of the solar cosmic rays above 10 MeV came from only 8 major active centers during solar cycle 19. Four of these were associated with this one particular location. If a "hot" region exists and can be identified early in a solar cycle, the prediction of large events would likely be associated with this one region.

According to Weddell [13], there seems to be a linear correlation between the smoothed sunspot number and the number of cosmic ray events, and also with the integrated intensity of particles above 10 MeV. Following Gleissberg [14], the probability is 95 percent that the maximum smoothed sunspot number for cycle 20 will not exceed 88^* ; whereas, the maximum sunspot number for cycle 19 was about 190. From the results of Waldmeier [15], the ascent time (defined as the time from minimum to maximum sunspot number) for solar cycle 20 should be about 4.5 years if the maximum sunspot number is 88. Thus, if the solar minimum occurred on July 1964, the maximum for cycle 20 should occur about January 1969. According to Weddell [13] and Webber [7], the number of annual particle events occurring at the next solar maximum should be about 4 or 5, with an annual integrated intensity above 10 MeV of about 10^9 particles per square centimeter, based on results of solar cycle 19.

The distribution of the integrated flux per event [13] as a function of the number of events for cycle 19 is given in Figure 14. The monthly probabilities of events as a function of event size over the 96-month period from 1956 through 1963 for 68 flare events is shown in Figure 15.

It is also observed from tabulated data that during solar cycles from 1942 through 1963 (covering 76 observed events [13]), July was by far the most active month, with 18.4 percent; and August the third, with 13.2 percent. December, with no observed events, has apparently been the least active month.

* More recent calculations indicate that the smoothed sunspot number for cycle 20 may be as high as 150.

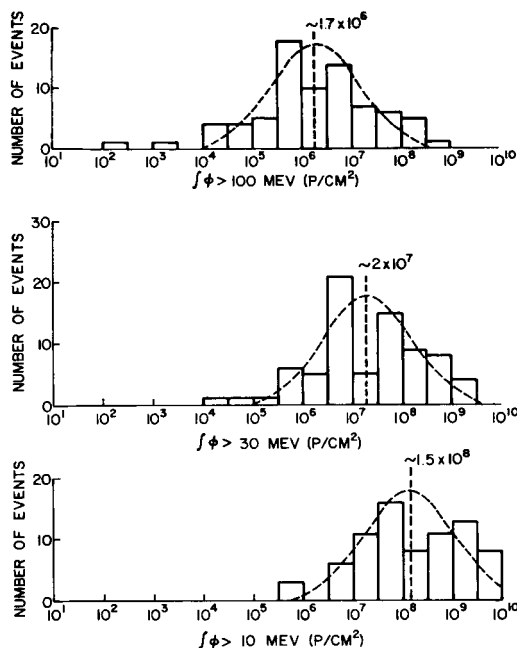


FIGURE 14. DISTRIBUTION OF THE INTEGRATED FLUX PER EVENT AS A FUNCTION OF THE NUMBER OF EVENTS FOR SOLAR CYCLE 19 (TAKEN FROM [13])

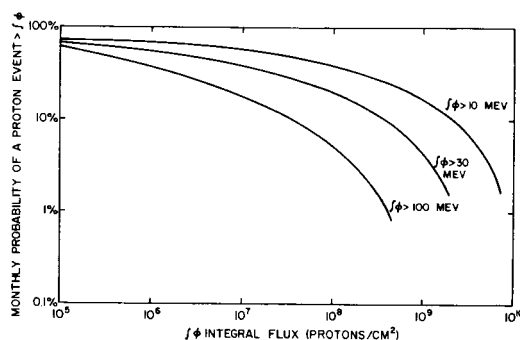


FIGURE 15. MONTHLY PROBABILITY OF A PROTON EVENT AS A FUNCTION OF EVENT SIZE (TAKEN FROM [13])

In conclusion, the authors of this paper would like to point out that the above "shotgun" treatment of solar flare prediction is primarily for familiarization purposes. For more definitive treatments, the indicated references should be consulted.

TRAPPED PROTON RADIATION

The proton environmental data used in this study was taken from the work of James I. Vette [16] of Aerospace Corporation. The proton flux above four different threshold energies is shown in Figures 16 through 19. These fluxes are for circular orbits at different altitudes above the earth for 0, 30, 60, and 90-degrees, respectively. The skin dose rates calculated from the AP3 spectral data are shown in Figures 20 through 23. The AP3 data was extended down to 40 MeV to obtain the proton dose rates for the 2 gram-per-square-centimeter cases.

The above proton dose calculations [8] include primary and secondary particles, and the dose is computed for a point at the center of a spherical shell of indicated shield thickness. No self-shielding by astronauts is included; hence, doses are high by approximately a factor of two for human targets.

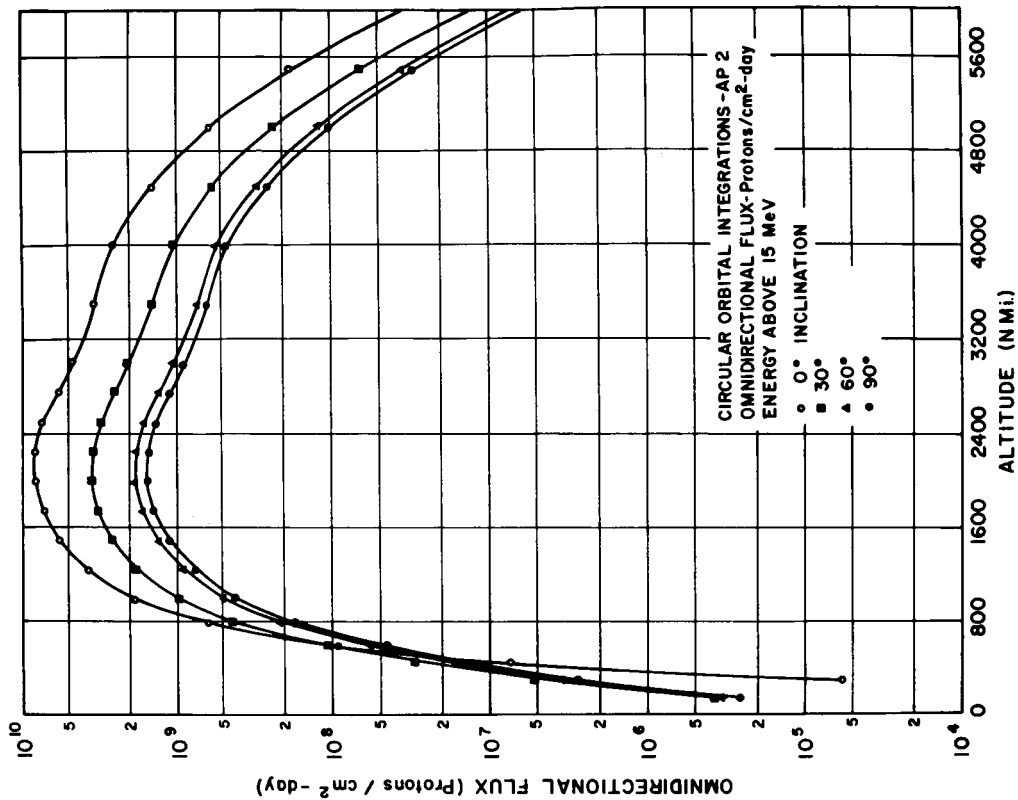


FIGURE 17. TRAPPED OMNIDIRECTIONAL
PROTON FLUX ABOVE 15 MeV

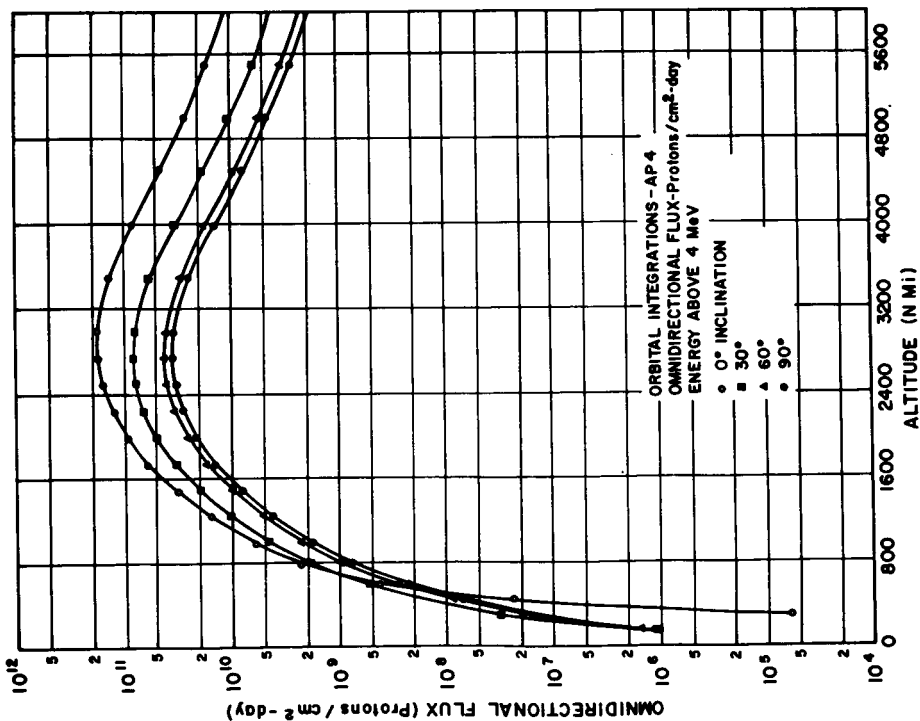


FIGURE 16. TRAPPED OMNIDIRECTIONAL
PROTON FLUX ABOVE 4 MeV

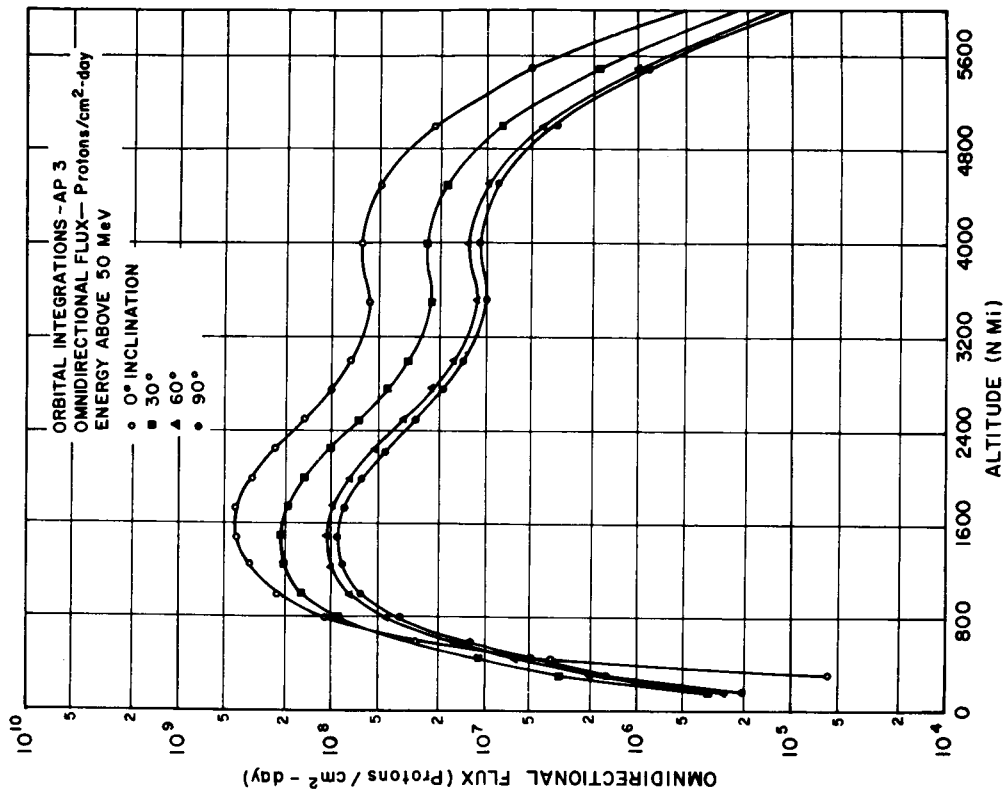


FIGURE 18. TRAPPED OMNIDIRECTIONAL
PROTON FLUX ABOVE 34 MeV

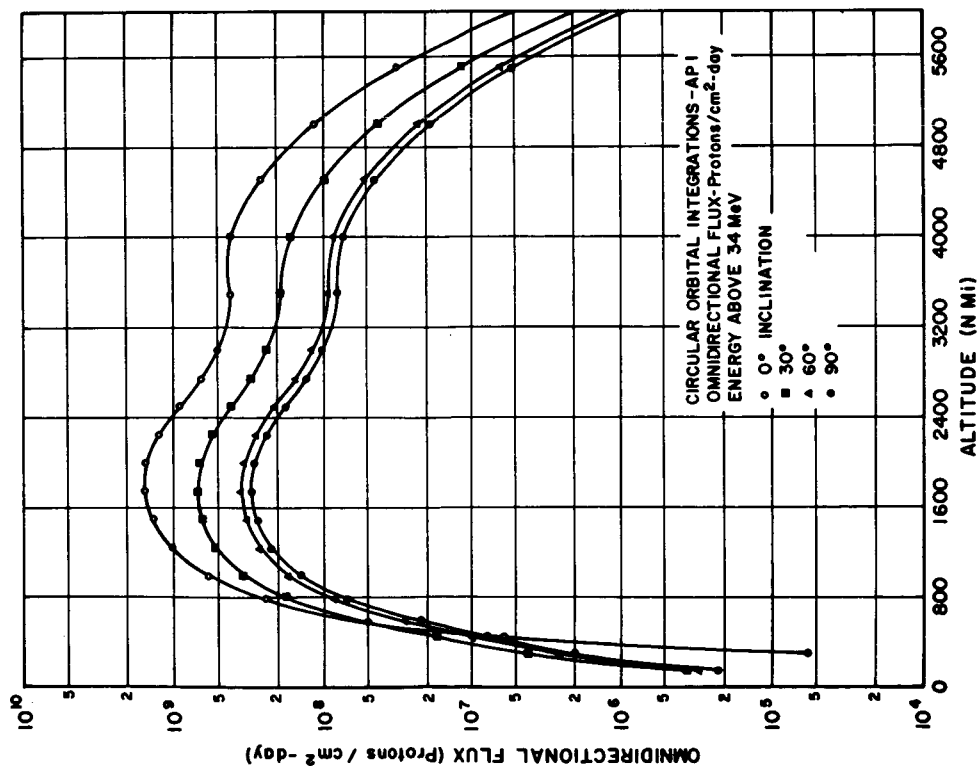


FIGURE 19. TRAPPED OMNIDIRECTIONAL
PROTON FLUX ABOVE 50 MeV

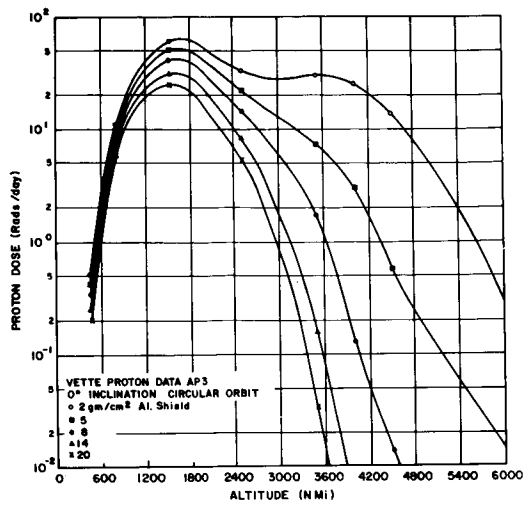


FIGURE 20. TRAPPED PROTON DOSE RATE AS A FUNCTION OF SHIELD THICKNESS AND ALTITUDE FOR 0-DEGREE INCLINATION

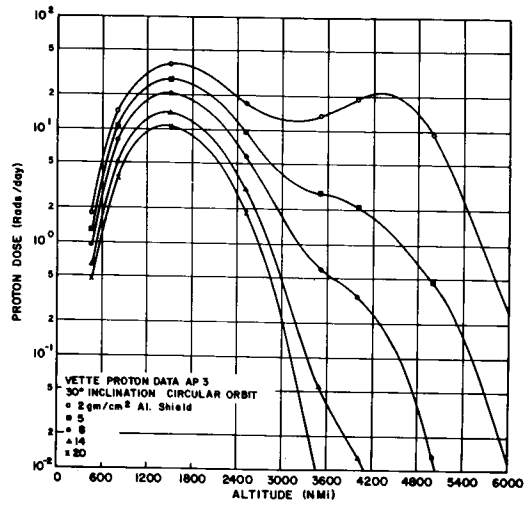


FIGURE 21. TRAPPED PROTON DOSE RATE AS A FUNCTION OF SHIELD THICKNESS AND ALTITUDE FOR 30-DEGREE INCLINATION

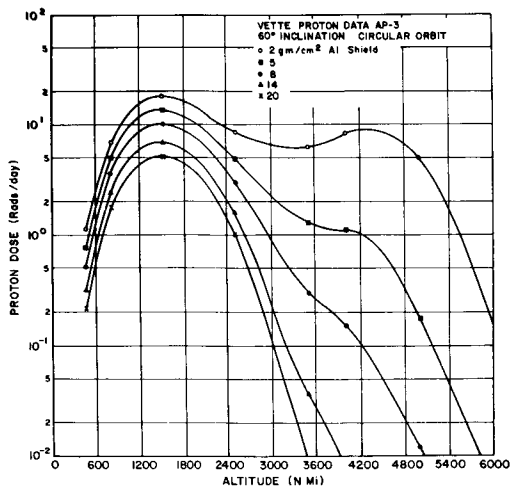


FIGURE 22. TRAPPED PROTON DOSE RATE AS A FUNCTION OF SHIELD THICKNESS AND ALTITUDE FOR 60-DEGREE INCLINATION

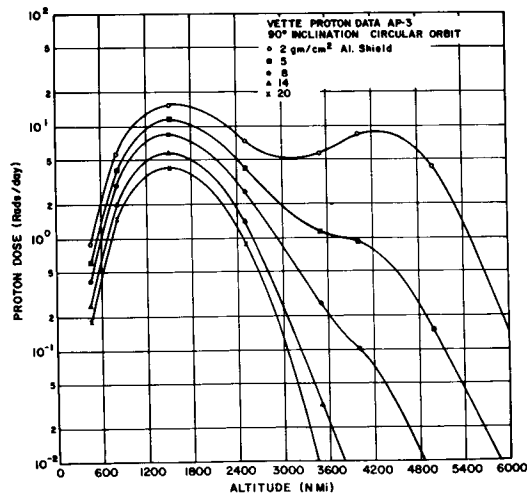


FIGURE 23. TRAPPED PROTON DOSE RATE AS A FUNCTION OF SHIELD THICKNESS AND ALTITUDE FOR 90-DEGREE INCLINATION

TRAPPED ELECTRON AND BREMSSTRAHLUNG RADIATION

Figure 24 is a plot of the trapped electron flux for circular orbits as a function of altitude and orbital inclination during August 1964. The electron environmental data were also taken from the work of J. I. Vette [16].

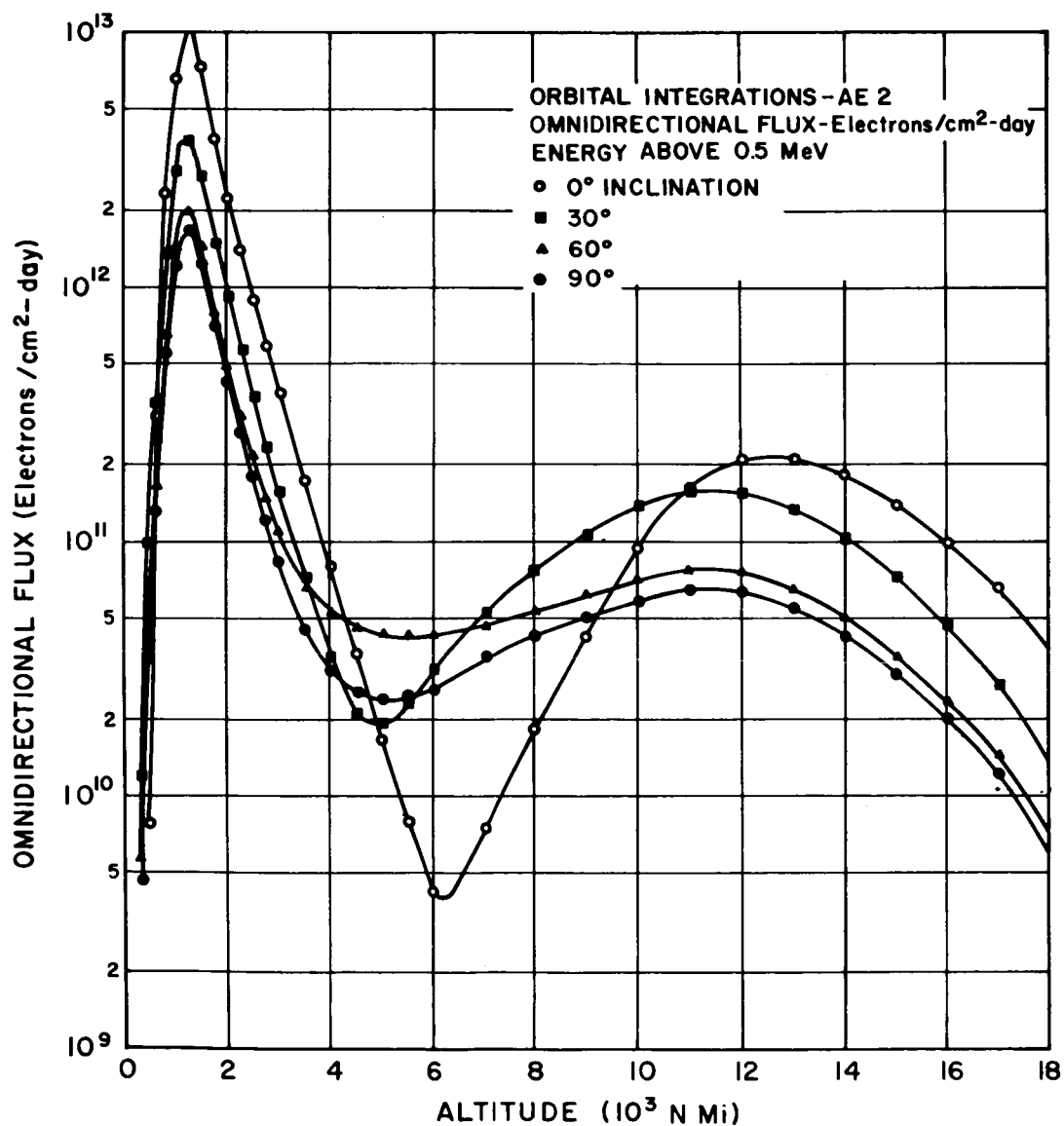


FIGURE 24. TRAPPED ELECTRON FLUX FOR CIRCULAR ORBITS
AS A FUNCTION OF ALTITUDE AND ORBIT INCLINATION

The electron dose rate at the center of a spherical shell corresponding to these data are plotted in Figures 25 through 28 as a function of aluminum shield thickness and altitude above the earth for orbit inclinations of 0, 30, 60, and 90 degrees, respectively. The electrons are assumed to be isotropically incident on the shield. Since these dose rate calculations do not include self-shielding, they are high by about a factor of two for the astronaut.

Using the above electron data, the bremsstrahlung* dose rate at the center of a sphere for an isotropic incident electron flux is given in Figures 29 through 32. For shields greater than about one gram per square centimeter, the bremsstrahlung dose is the most important radiation hazard for orbital missions, except at the altitudes where the proton belts are intense.

A typical bremsstrahlung dose transmission curve is shown in Figure 33 for isotropically incident electrons with an energy spectrum given by

$$\phi(>E) = 10^{13} \exp(-2E) \frac{\text{electrons}}{\text{cm}^2 - \text{day}} \quad (11)$$

The bremsstrahlung dose is not strongly dependent on aluminum thickness, as shown in Figure 33. However, the bremsstrahlung dose is primarily from low energy X-rays whose intensity could be greatly reduced by adding a thin layer of lead on the inside of the shield.

The electron dose rate as a function of shield thickness is shown in Figure 34 for a model electron integral spectrum given by

$$\phi(>E) = N_0 \exp\left(-\frac{E}{E_0}\right) \quad (12)$$

with $\phi(>0.5) = 10^{10}$ electrons-per-square-centimeter-day and the values of E_0 are chosen between 0.25 and 1.25.

It is important to have some feeling for the possible dose values received from the trapped electron environment during the solar maximum of solar cycle 20. Vette [16] has produced a possible projected electron environment for December 1968 (Fig. 35), for orbit inclinations 0, 30, 60 and 90 degrees. He has decayed the inner electron belt according to the measurements of Bostrom, et al. [17], and increased the intensity of the outer electron belt to correspond to solar maximum conditions. Using the above projected energy spectra data, the projected electron dose rate as a function of altitude and shield thickness is

* Bremsstrahlung are continuous spectra X-rays produced by the inelastic collision of electrons with nuclei.

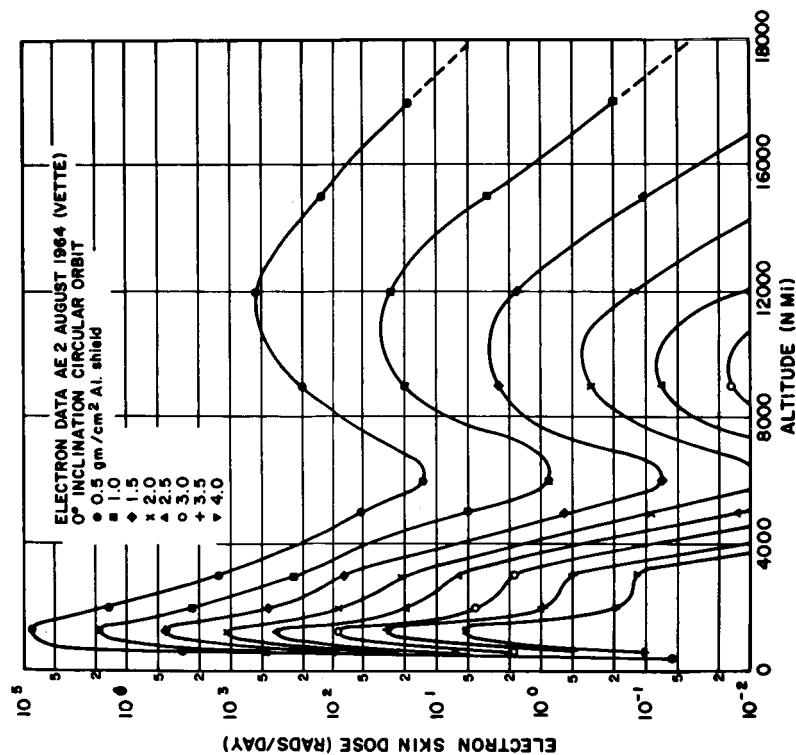


FIGURE 25. ELECTRON DOSE RATE AS A
FUNCTION OF ALTITUDE AND SHIELD THICKNESS
FOR 0-DEGREE INCLINATION

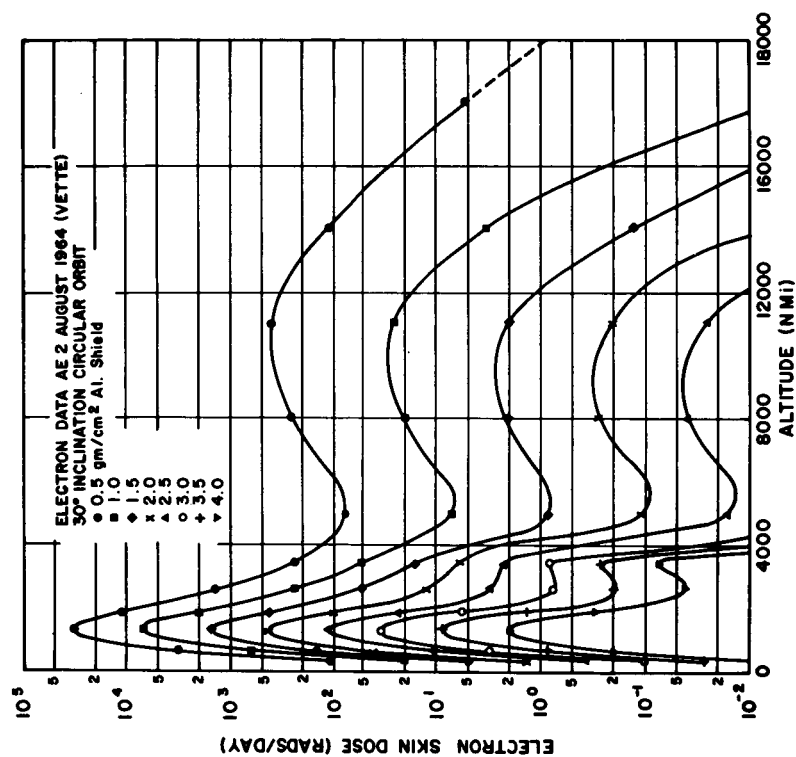


FIGURE 26. ELECTRON DOSE RATE AS A
FUNCTION OF ALTITUDE AND SHIELD THICKNESS
FOR 30-DEGREE INCLINATION

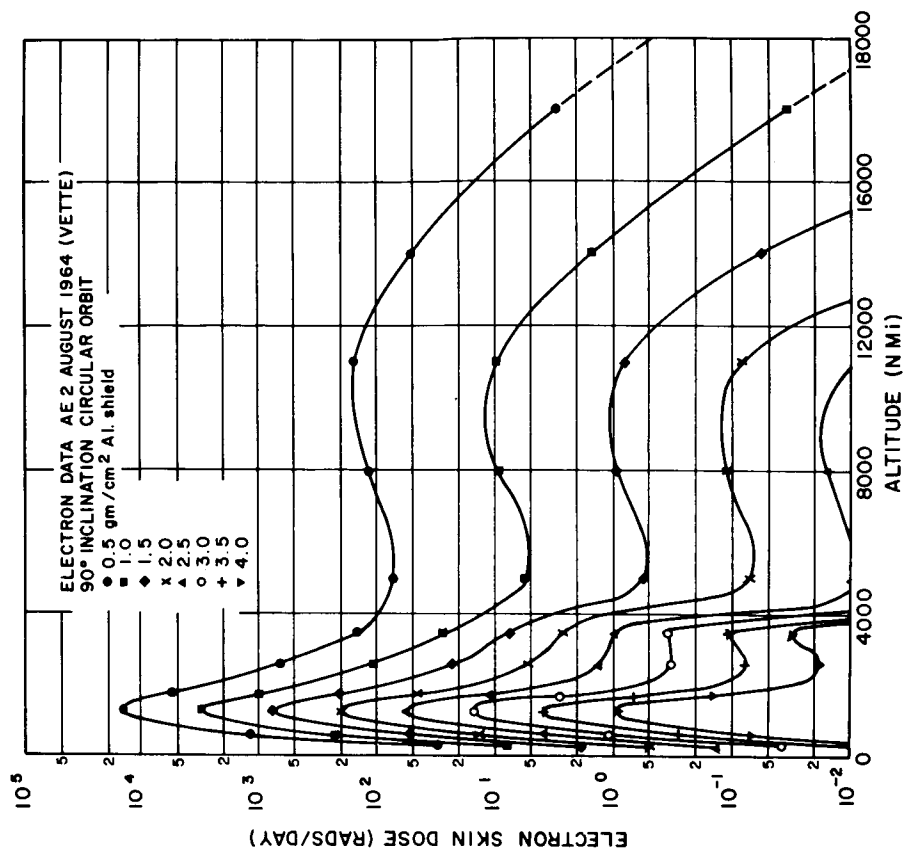


FIGURE 27. ELECTRON DOSE RATE AS A
FUNCTION OF ALTITUDE AND SHIELD THICKNESS
FOR 60-DEGREE INCLINATION

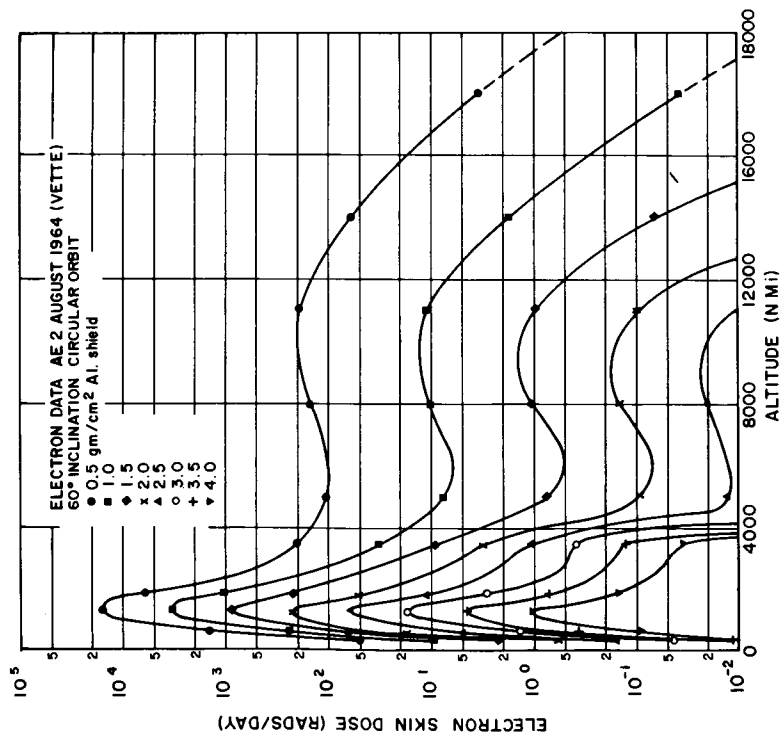


FIGURE 28. ELECTRON DOSE RATE AS A
FUNCTION OF ALTITUDE AND SHIELD THICKNESS
FOR 90-DEGREE INCLINATION

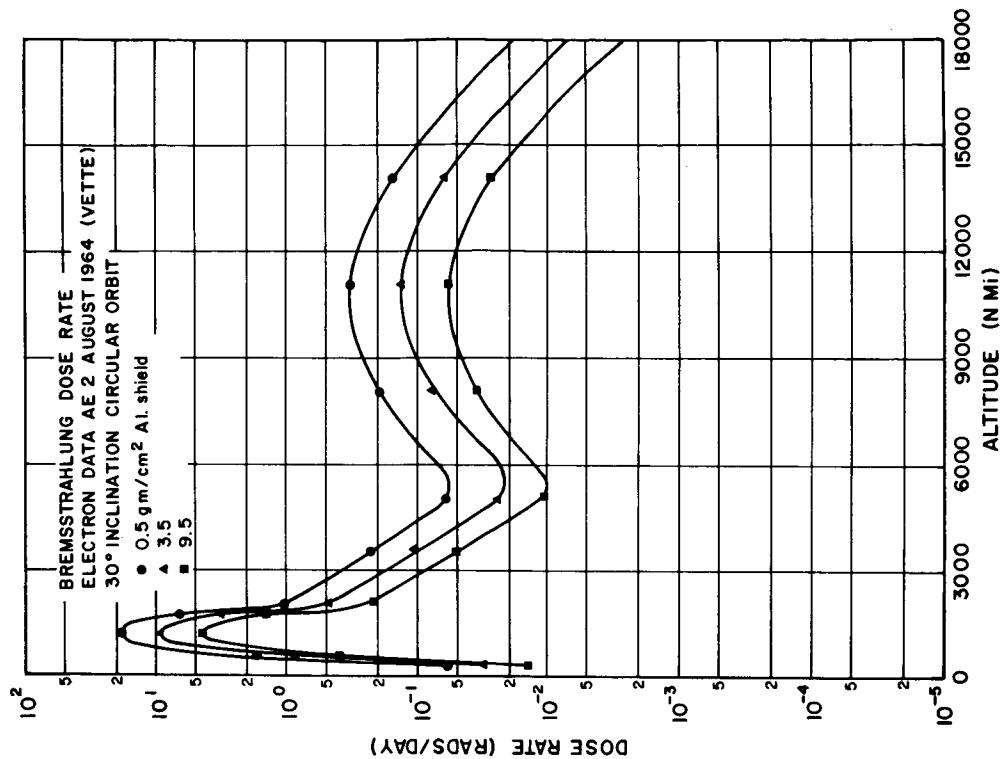


FIGURE 30. BREMSSTRAHLUNG DOSE RATE AS A FUNCTION OF SHIELD THICKNESS AND ALTITUDE FOR 30-DEGREE INCLINATION

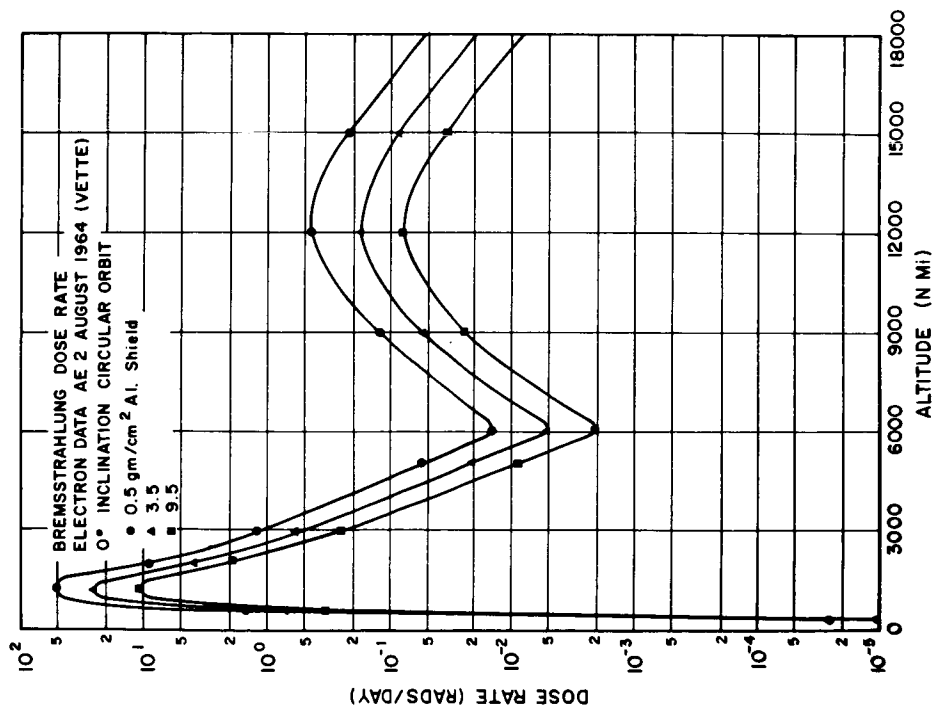


FIGURE 29. BREMSSTRAHLUNG DOSE RATE AS A FUNCTION OF SHIELD THICKNESS AND ALTITUDE FOR 0-DEGREE INCLINATION

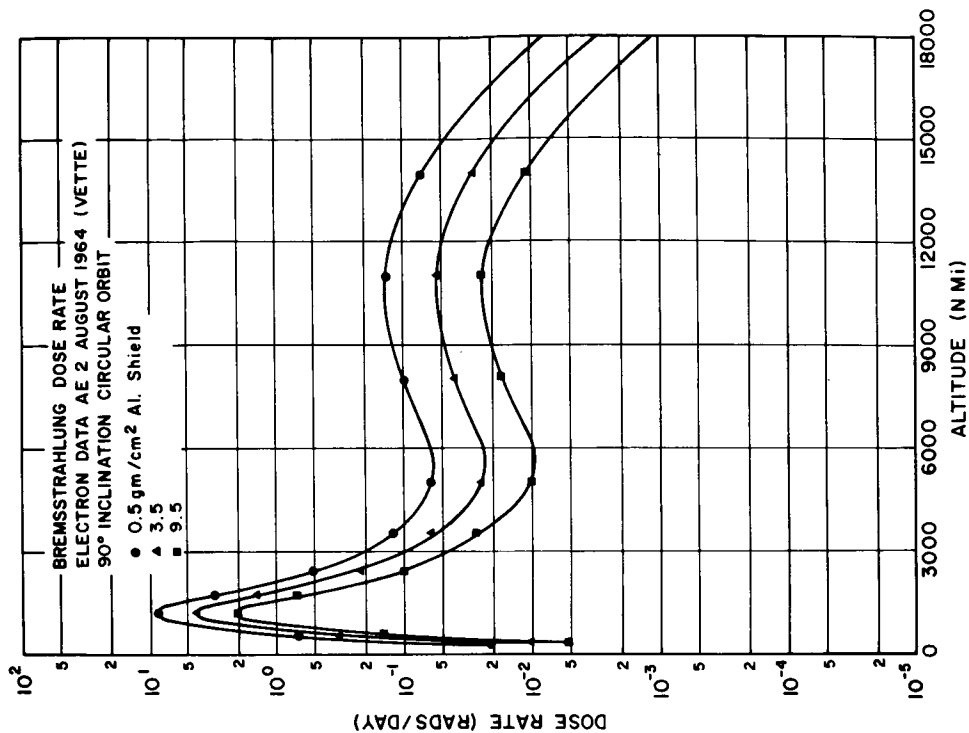


FIGURE 31. BREMSSTRAHLUNG DOSE RATE AS A FUNCTION OF SHIELD THICKNESS AND ALTITUDE FOR 60-DEGREE INCLINATION

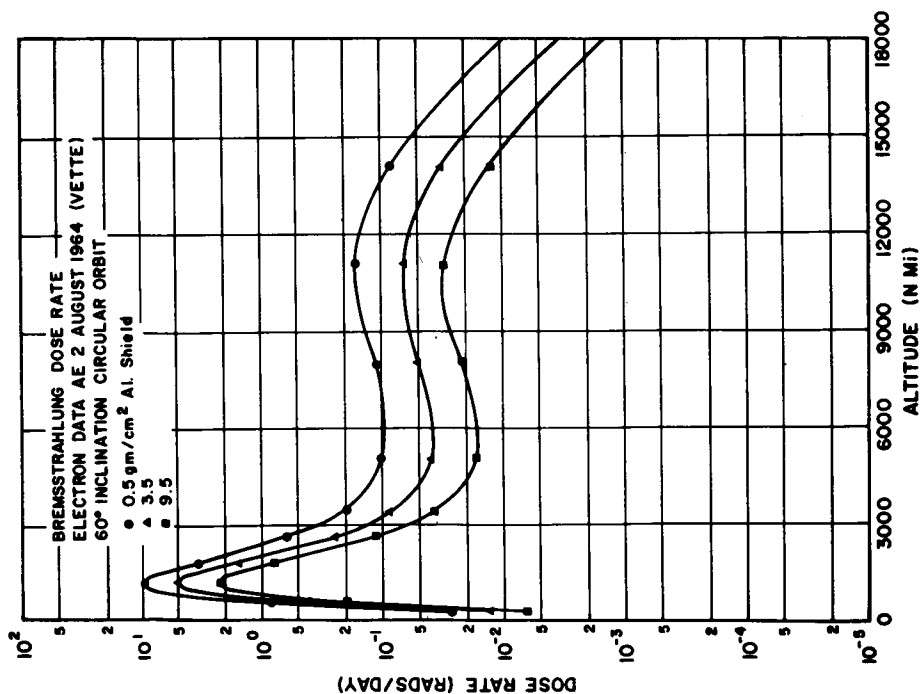


FIGURE 32. BREMSSTRAHLUNG DOSE RATE AS A FUNCTION OF SHIELD THICKNESS AND ALTITUDE FOR 90-DEGREE INCLINATION

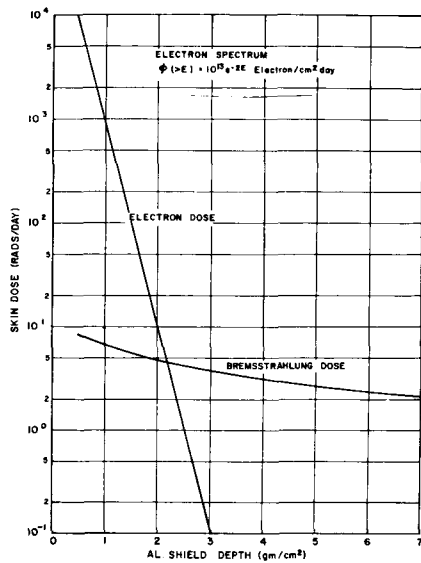


FIGURE 33. ELECTRON AND BREMSSTRAHLUNG DOSE RATE AS A FUNCTION OF SHIELD THICKNESS USING A TYPICAL ELECTRON INTEGRAL SPECTRUM

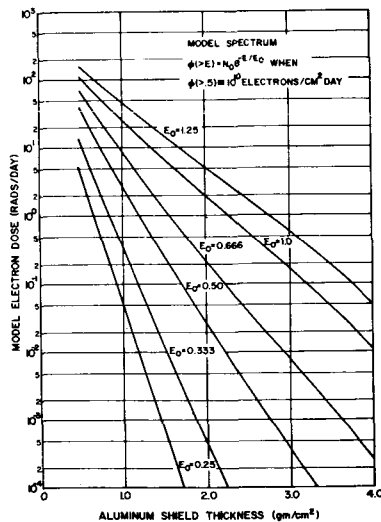


FIGURE 34. ELECTRON DOSE RATE AS A FUNCTION OF SHIELD THICKNESS FOR SEVERAL CHARACTERISTIC E_0 VALUES

plotted in Figures 36 through 39 for inclinations of 0, 30, 60, and 90 degrees. The corresponding projected bremsstrahlung dose rate calculations for 1968 are depicted in Figures 40 through 43.

CONCLUSIONS

The results presented in this report should be of practical value for preliminary engineering analysis of space hazards and planning of possible space missions for either near-earth orbits or deep-space probes. The dose rate curves shown in this report are based on the latest environmental analysis by NASA and the United States Air Force. The environmental models and data will be continually updated as knowledge increases from better experimental data and more sophisticated analysis. As such modifications become available, the authors of this report intend to update the radiation dose rate analysis in future reports. This is pertinent for the synchronous orbit radiation environment which is now being examined in greater detail by experimental space probes and theoretical analysis.

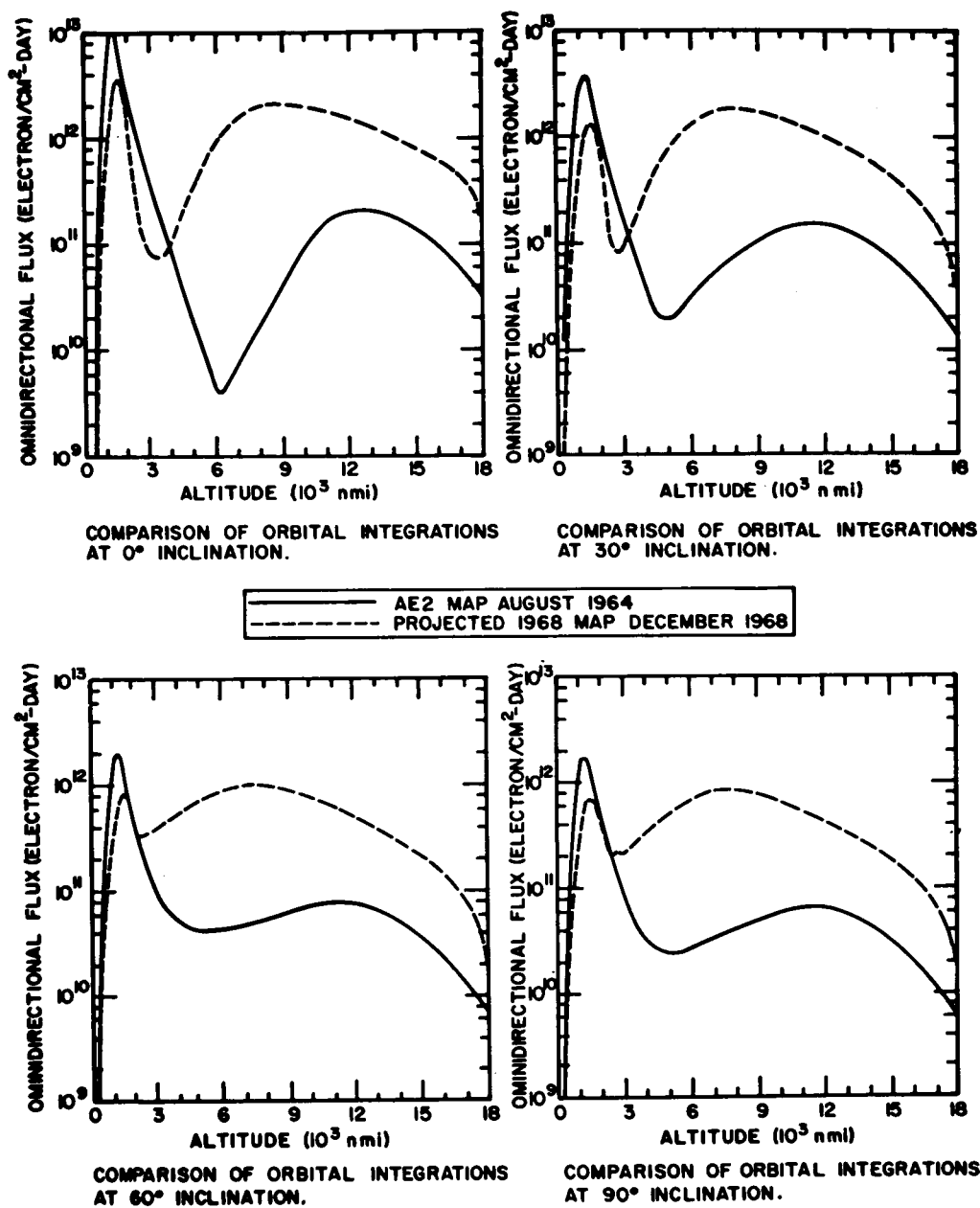


FIGURE 35. PROJECTED ELECTRON ENVIRONMENT FOR DECEMBER 1968

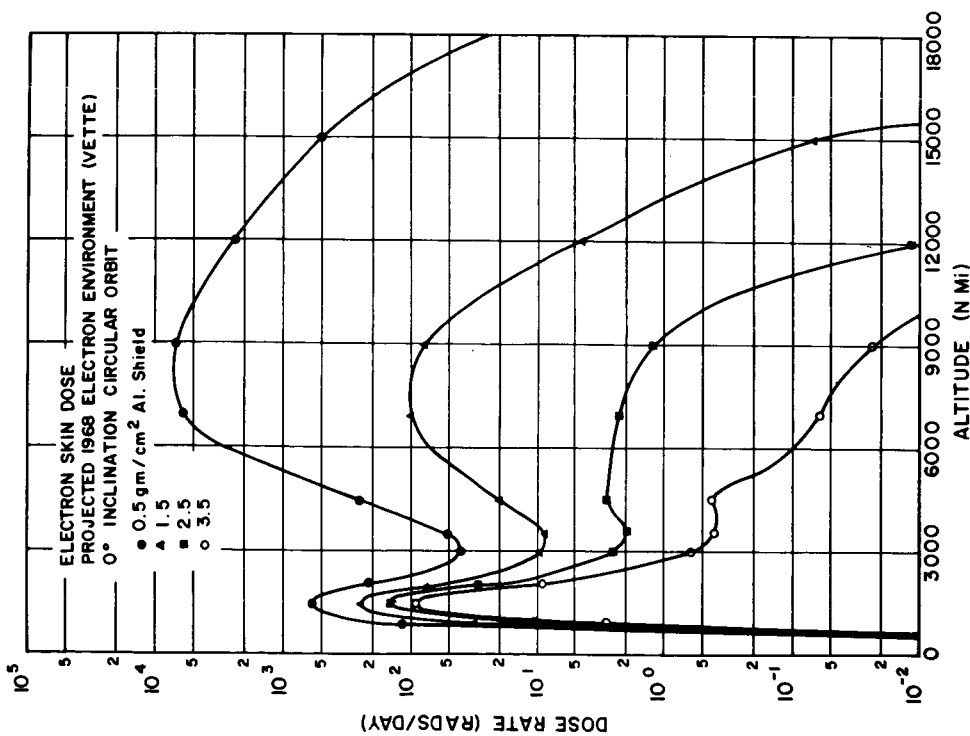


FIGURE 36. PROJECTED ELECTRON DOSE RATE AS A FUNCTION OF ALTITUDE AND SHIELD THICKNESS FOR 0-DEGREE INCLINATION

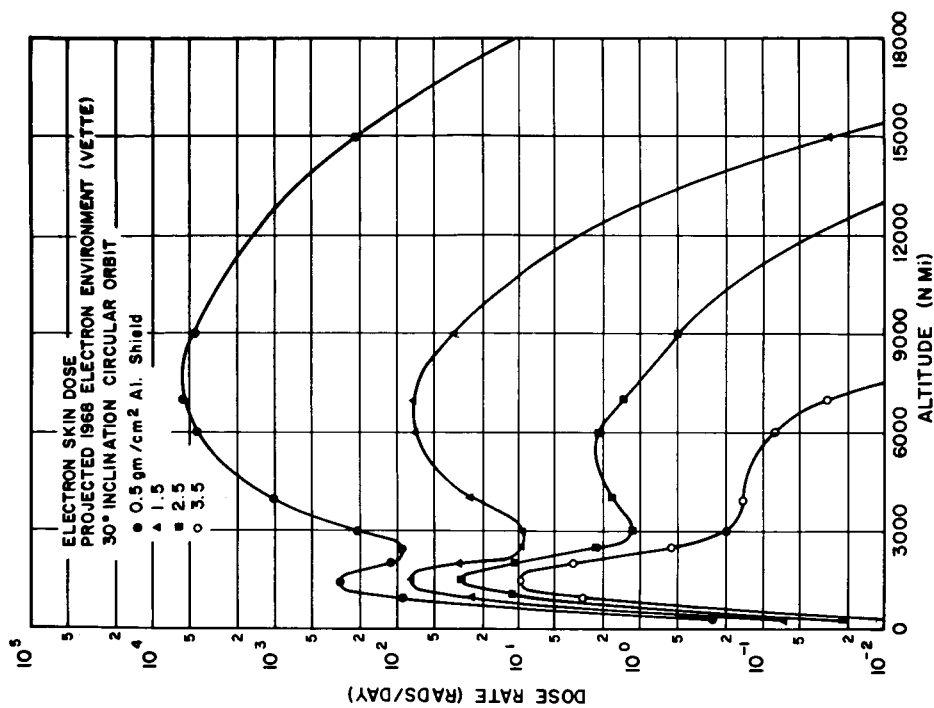


FIGURE 37. PROJECTED ELECTRON DOSE RATE AS A FUNCTION OF ALTITUDE AND SHIELD THICKNESS FOR 30-DEGREE INCLINATION

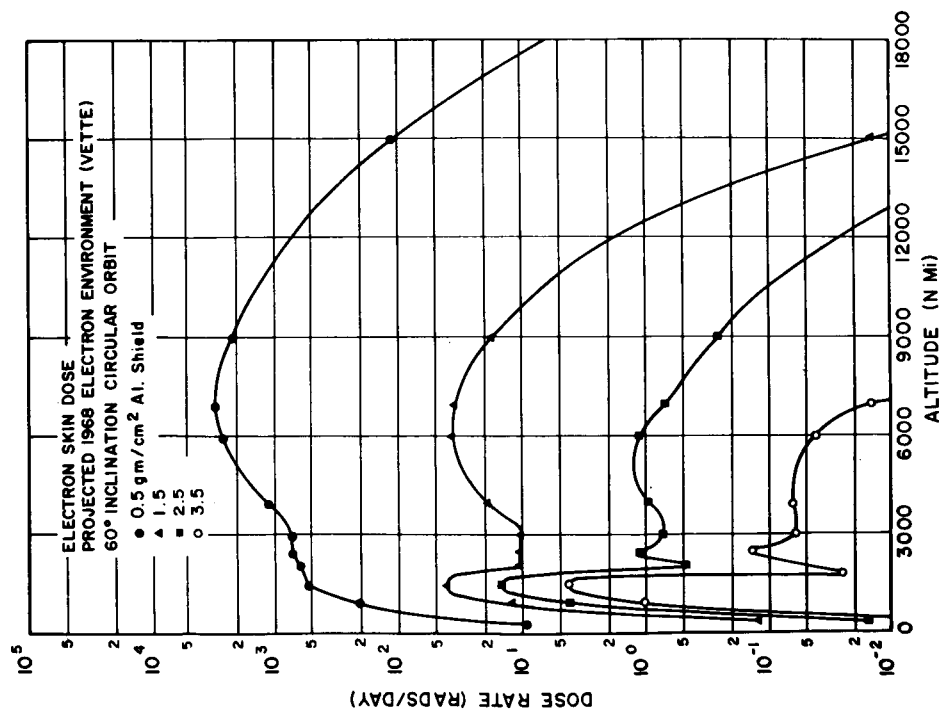


FIGURE 38. PROJECTED ELECTRON DOSE RATE AS A FUNCTION OF ALTITUDE AND SHIELD THICKNESS FOR 60-DEGREE INCLINATION

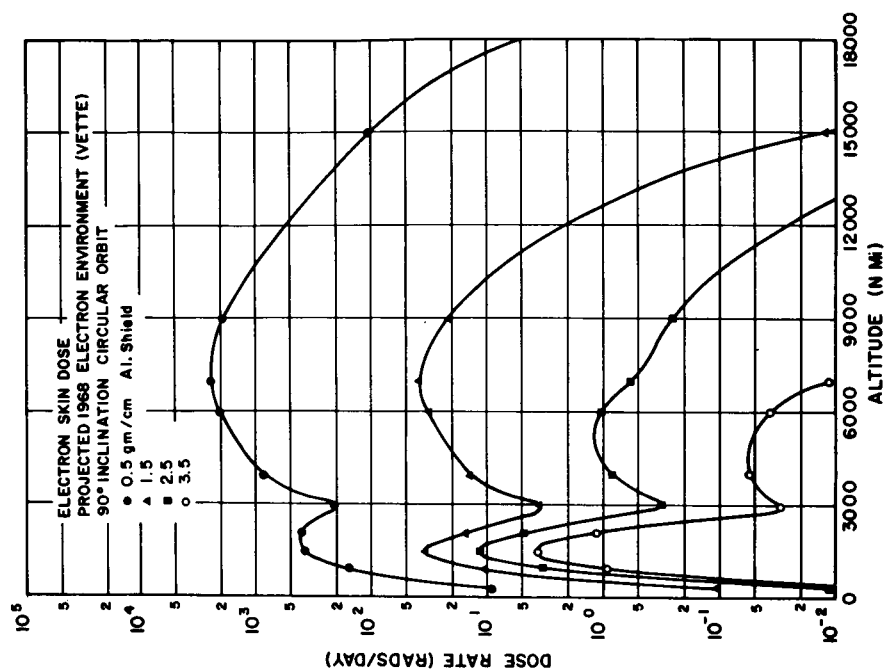


FIGURE 39. PROJECTED ELECTRON DOSE RATE AS A FUNCTION OF ALTITUDE AND SHIELD THICKNESS FOR 90-DEGREE INCLINATION

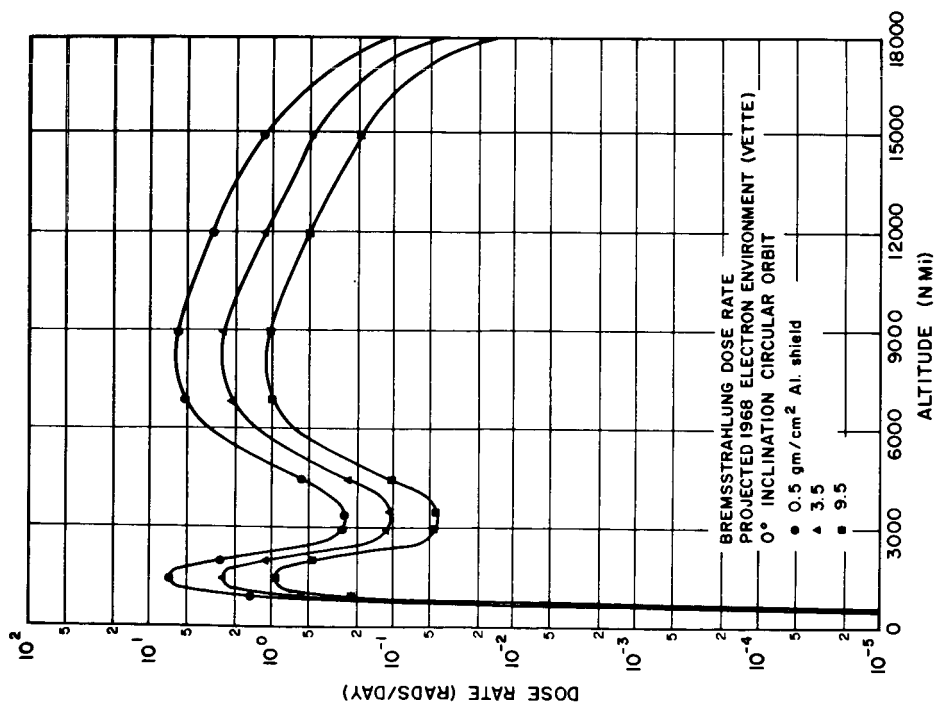


FIGURE 40. PROJECTED BREMSSTRAHLUNG DOSE RATE AS A FUNCTION OF ALTITUDE AND SHIELD THICKNESS FOR 0-DEGREE INCLINATION

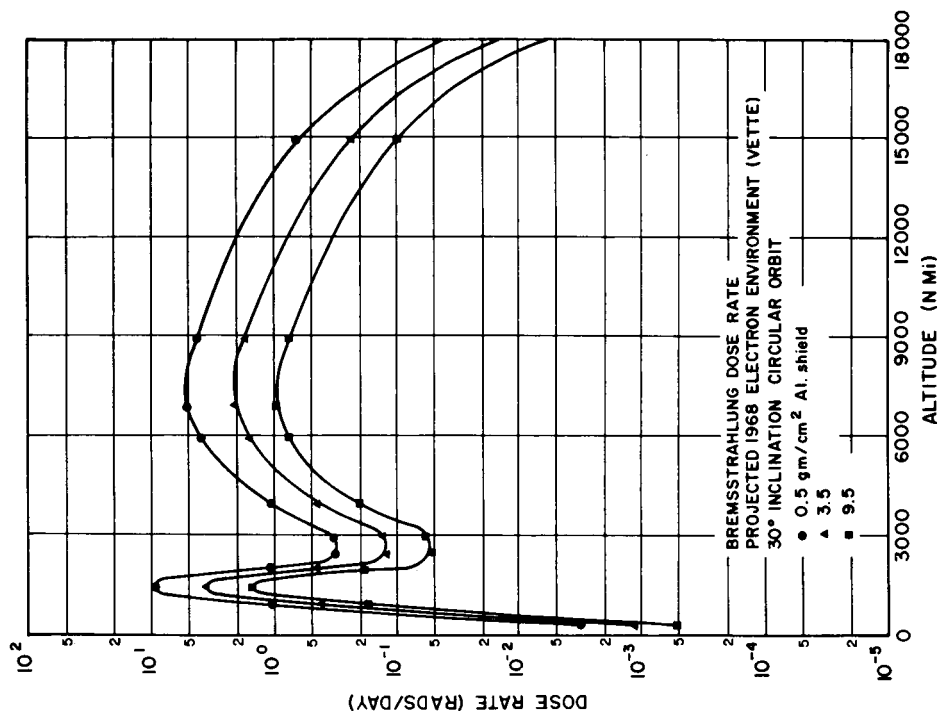


FIGURE 41. PROJECTED BREMSSTRAHLUNG DOSE RATE AS A FUNCTION OF ALTITUDE AND SHIELD THICKNESS FOR 30-DEGREE INCLINATION

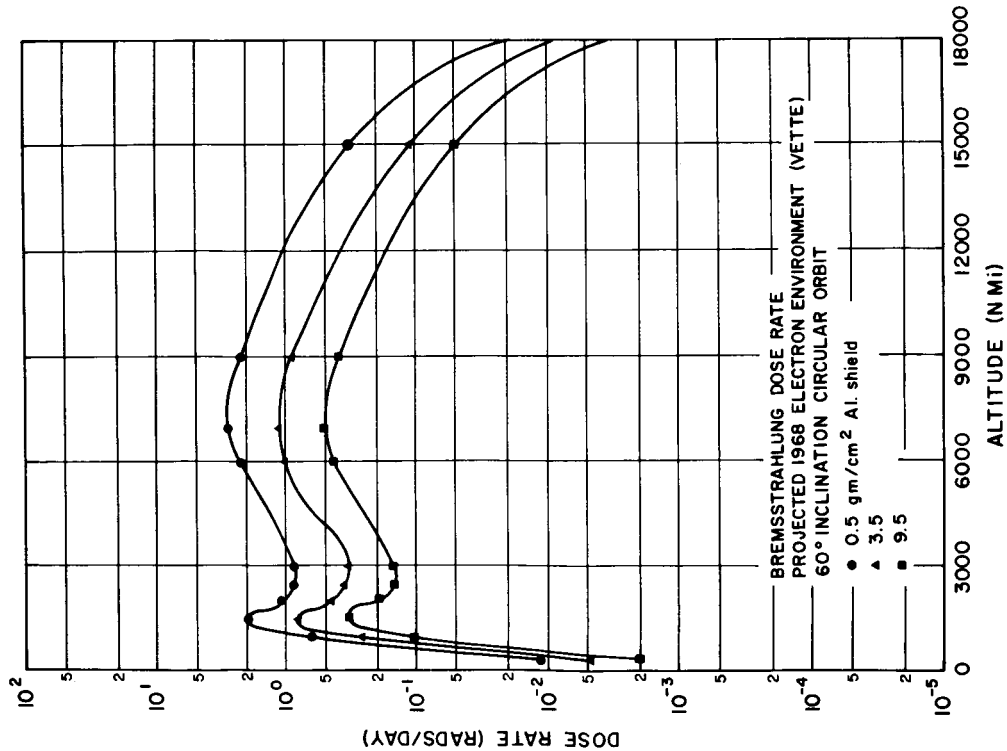


FIGURE 42. PROJECTED BREMSSTRAHLUNG DOSE RATE AS A FUNCTION OF ALTITUDE AND SHIELD THICKNESS FOR 60-DEGREE INCLINATION

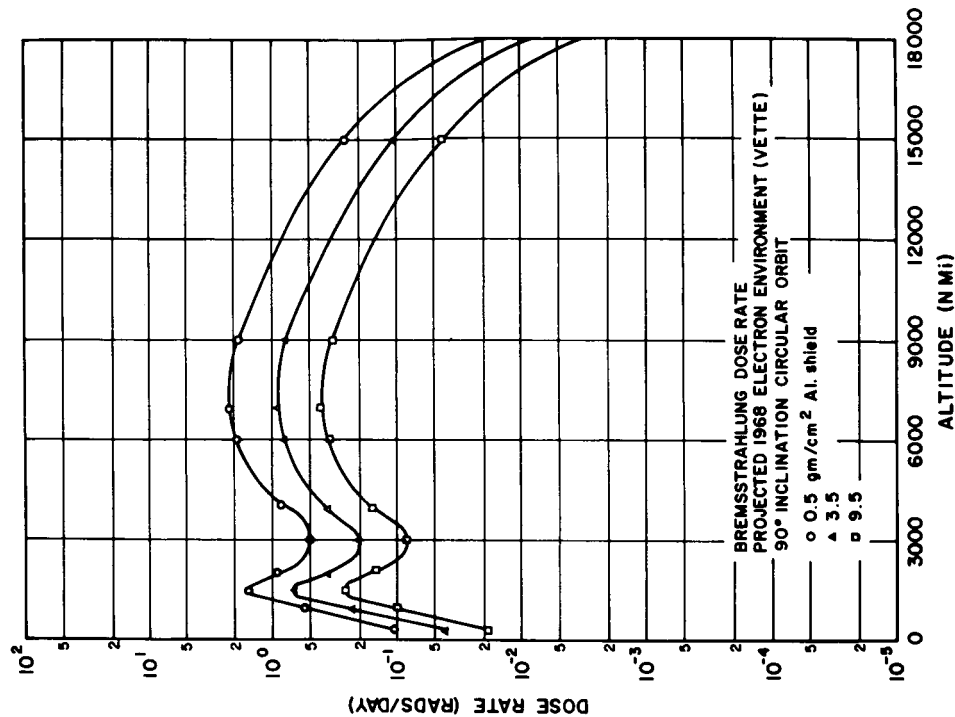


FIGURE 43. PROJECTED BREMSSTRAHLUNG DOSE RATE AS A FUNCTION OF ALTITUDE AND SHIELD THICKNESS FOR 90-DEGREE INCLINATION

REFERENCES

1. Ness, N. F.: The Earth's Magnetic Tail. J. Geophys. Res., 70, 2984, 1965.
2. McIlwain, C. E.: Coordinates for Mapping the Distribution of Magnetically Trapped Particles. J. Geophys. Res., vol. 66, no. 11, Nov. 1961.
3. Störmer, C.: Polar Aurora. Oxford University Press, London, 1955.
4. Fermi, E.: Nuclear Physics Chapter X. University of Chicago Press, Chicago, 1949.
5. _____: Computer Codes for Space Radiation Environment and Shielding. Rep. WL T DR-64-71, Vol. I, The Boeing Co.
6. Fichtel, C. E.; Guss, D. E.; Kniffen, D. A.; and Neelakantan, K. A.: Modulation of Low-energy Galactic Cosmic-ray Hydrogen and Helium. J. Geophys. Res., vol. 69, no. 15, pp. 3293-3295, August 1, 1964.
7. Webber, W. R.: An Evaluation of the Radiation Hazard Due to Solar Particle Events. Document D2-90469, The Boeing Co., December 1963.
8. Burrell, M. O.: The Calculation of Proton Penetration and Dose Rates. NASA TM X-53063, August 17, 1964.
9. Baker, M. B.: Geomagnetically Trapped Radiation. Rep. SM-47635, Douglas Aircraft Corp., October 1964.
10. Hill, C. W.; Ritchie, W. B.; and Simpson, K. M.: Data Compilation and Evaluation of Space Shielding Problems. Vol. 3, Rep. ER7777, Lockheed Co., April 1966.
11. Webber, W. R.: An Evaluation of Solar Cosmic Ray Events During Solar Minimum. Document D2-84274-1, The Boeing Co., June 1966.
12. Guss, D. E.: Distribution in Heliographic Longitude of Flares Which Produce Energetic Solar Particles. Phys. Rev. Letters, 13, p. 363, 1964.

REFERENCES (Concluded)

13. Weddell, J. B.; Haffner, J. W.; and Morin, F. J.: Statistical Evaluation of Proton Radiation from Solar Flares. Rep. SIB 66-421, North American Aviation, Inc., May 20, 1966.
14. Gleissberg, W.: The Character of the Next Sunspot Maximum. *Zeitschrift fur Astrophysik*, 49, 25, 1960.
15. Waldmeier, M.: Prognose fur das Naschste Sonnenfleckenmaximum. *Astron. Nachr.*, 259, 267, 1936.
16. Vette, J. I.; et al.: Models of the Trapped Radiation Environment. Vols. 1 and 2, NASA SP-3024, 1966.
17. Bostrom, C. O.; Williams, D. J.; and Beall, D. S.: Time Decay of the Artificial Radiation Belt. *Trans. Am. Geophys. Union*, Vol. 46, 137, 1965.

A PRELIMINARY REPORT ON ENERGETIC SPACE
RADIATION AND DOSE RATE ANALYSIS

By M. O. Burrell, J. J. Wright and J. W. Watts

The information in this report has been reviewed for security classification. Review of any information concerning Department of Defense or Atomic Energy Commission programs has been made by the MSFC Security Classification Officer. This report, in its entirety, has been determined to be unclassified.

This report has also been reviewed and approved for technical accuracy.

A handwritten signature in cursive script, reading "Ernst Stuhlinger", is written over a horizontal line.

ERNST STUHLINGER

Director, Research Projects Laboratory

DISTRIBUTION

INTERNAL

DIR

Dr. von Braun

R-RP

Dr. Stuhlinger
Mr. Heller
Dr. Shelton
Dr. Johnson
Mr. Robinson
Mr. Downey
Mr. Miles
Mr. Urban
Mr. Duncan
Dr. Dozier
Mr. Holland
Dr. Hale
Dr. Seitz
Dr. Wood
Mr. Potter
Mr. Burrell (10)
Mr. Wright (10)
Dr. Edmonson
Mr. Stern
Mr. Watts
Reserve (50)

R-AERO

Dr. Geissler
Mr. Roberts
Mr. Smith
Mr. Vaughan

R-COMP

Dr. Hoelzer

R-QUAL

Mr. Schulze
Dr. Grau

AS-VL

Mr. Bill Powers (3)

R-ME

Dr. Kuers

R-TEST

Mr. Heimburg

R-ASTR

Dr. Haeusserman

LVO-DIR

Dr. Debus

R-P& VE

Mr. Jordan

MS-IP

MS-IP (8)

CC-P

I-RM-M

MS-H

EXTERNAL

Scientific and Technical Information

Facility (25)

ATTN: NASA Representative (S-AK/RKT)

P. O. Box 33

College Park, Maryland 20740

NASA Headquarters

National Aeronautics and Space
Administration

Washington, D. C. 20546

Code RV-1

Mr. J. Warren Keller
Mr. Charles T. D'Aiutolo
Mr. Clotaire Wood
Mr. Arthur Reetz (5)

DISTRIBUTION (Concluded)

EXTERNAL (Concluded)

Code MT	NASA Goddard Space Flight Center
Mr. Nathaniel B. Cohen	Greenbelt, Maryland 20771
Code SC	Dr. Wilmot Hess
Dr. John T. Holloway	Dr. Leslie Meredith
Code SS	Dr. Robert Jastrow, Director
Dr. John F. Clark	Goddard Institute of Space Studies
Code SG	National Aeronautics & Space
Dr. John E. Naugle	Administration
Mr. Maurice Dubin	475 Riverside Drive
Dr. Robert Fellows	New York, New York 10023
NASA Manned Spacecraft Center	Dr. Fred Singer
P. O. Box 1537	National Weather Satellite Center
Houston, Texas 77001	Chief, U. S. Weather Bureau
Mr. Jerry Modisette	Washington, D. C.
Mr. Maxime A. Faget	Dr. Charles Lundquist, Assistant
NASA Lewis Research Center	Director
21000 Brookpark Road	Smithsonian Astrophysical Observatory
Cleveland, Ohio 44135	60 Garden Street
Mr. Wolfgang E. Moeckel, Code 2200	Cambridge 38, Mass.
Dr. John C. Evvard, Code 2000	Dr. Fred Whipple, Director
NASA Ames Research Center	Smithsonian Astrophysical Observatory
Moffet Field, California	60 Garden Street
Mountain View, California 94035	Cambridge 38, Mass.
Dr. Smith J. De France, Director	
Mr. Don Gault	
NASA Langley Research Center	
Langley Field, Virginia	
Hampton, Virginia 23365	
Dr. John E. Duberg	
Dr. John S. Evans	
Dr. Trutz Foelsche	